An in-situ video technique for measuring drop size distributions in concentrated liquid-liquid dispersions

S.E. Kohn

Koninklijke/Shell-Laboratorium, Amsterdam

Delft, May 1996

Delft University of Technology
Faculty of Applied Physics
Kramers Laboratorium voor Fysische Technologie
Prins Bernhardlaan 6, 2628 BW Delft

Professor: prof.dr.ir. H.E.A. van den Akker
Supervisors: dr.ir. J.J. Derksen
ir. G.W. Colenbrander (Shell)
ir. P. Veenstra (Shell)

Summary

This report is concerned with drop size distributions of liquid-liquid dispersions in stirred tank reactors. The application of stirring immiscible liquids can be found in e.g., suspension polymerisation processes. Little is known about scaling up these processes. Industry is particularly interested in the scaling rules for the mean drop diameter and the width of the drop size distributions in such polymerisation reactions.

Experiments were performed to determine the influence of scaling and power input on the drop size distribution in liquid-liquid dispersions. The experiments were conducted in pilot scale vessels 1.8, 14.7 and 133.4 litre in size. For the continuous phase de-mineralised water is used, for the dispersed phase silicone oil (viscosity 5 mPa s, density 960 kg/m^3). The volume fraction dispersed phase was 50%. In each vessel 3 experiments were conducted, each with a different specific power input (0.2, 0.25 and 0.31 W/kg). Surfactants were added to overrule, in a controlled way, the effect of pollution on surface tension.

Drop size diameters were investigated with an intrusive optical measurement method that was developed for this research. The measurement method consisted of a CCD-camera fitted on an endoscope that was lowered in the dispersion. Drops ranging from 50 μm to 1.6 mm were measured with an error of 50 μm. The images, taken from inside the dispersion, were recorded on video to be analysed with image analysis.

A simulation program based on the Monte Carlo method was written to investigate the statistical accuracy of the measurement method and the amount of bias that is initiated by the optical technique. The program calculates the accuracy with which the width of a drop size distribution can be estimated given a certain number of drops.

Table of contents

1 Introduction

1.1 polystyrene

When leaving the factory raw expandable Polystyrene (EPS) consists of small spherical particles. The size varies between 250 μm and 2 mm. These particles will expand when treated with steam. As the particles also stick to each other, they can form any desired shape. In expanded form the polymer has unique characteristics. First of all the material has a very low density. It has an excellent shock absorbing capacity. Finally polystyrene has very good heat isolation properties. Because of these characteristics EPS is used in a wide variety of products: as base material for coffee cups, at the inside of crash helmets, in the isolation of roofs, in all kinds of floating objects and for the protection of transported consumer goods such as electronic equipment.

It is obvious that one needs a different kind of polystyrene for a coffee cup compared to polystyrene for the inside of a helmet. Therefore industry has very specific demands on the size and property of the raw expandable polystyrene.

1.2 The fabrication process of polystyrene

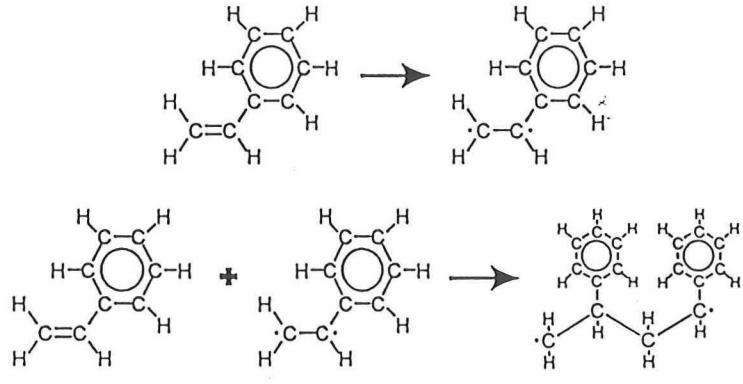

Figure 1.1 A simplified illustration of a step in the polymerisation process of styrene (up left)

Obviously, polystyrene is formed as the result of a polymerisation reaction. During the reaction a hydrocarbon molecule (initially a monomer) links to another monomer. This is accomplished through the formation of so called radicals (radicals are molecules with unbound electrons). Multiple polymerisation steps lead to a long molecule. The final material has a mean molecular weight

depending on the particular process conditions. Altering these conditions results in different products. A simplified illustration of a polymerisation reaction system for polystyrene is shown in Figure 1.1.

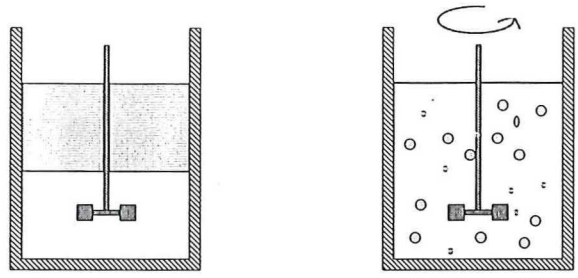

Figure 1.2 Illustration of two immiscible fluids being stirred.

The formation process is a so called suspension polymerisation process. It is a batch process in a stirred vessel. The typical volume of such an industrial scale vessel is between 30 to 50 m^3. First the vessel is filled with water. Then the monomer styrene is added. The volume ratio water/styrene is 1:1. Droplets are formed when the vessel is stirred as illustrated in Figure 1.2. This is because styrene is a-polar and does not dissolve in water. Comparable effects occur when water and oil are stirred. The water is the continuous phase while the styrene becomes the dispersed phase. Without agitating the two liquids, a phase separation will occur due to density differences between continuous phase and dispersed phase. After a fixed amount of time the reaction is started by adding radical makers and other substances. The viscosity of the drop increases until eventually it becomes an expandable polystyrene particle. The size of the initial styrene drop mainly determines the size of the final EPS particle.

1.3 Distributions; history and goal

At the end of the process described in section 1.2 the batch of EPS particles has a broad size distribution. Because of customer-demands on the bead size (that are characterised as grades), each different grade has a different price. In reality it proves to be very difficult to produce one batch of one grade only. Normally the bead size distribution is wider than the grade specification (see Figure 1.3). This asks for sieving the batch, which is costly. It can occur that there is virtually no demand for a specific unintended grade. In the latter case the EPS is sold below the production price or is destroyed.

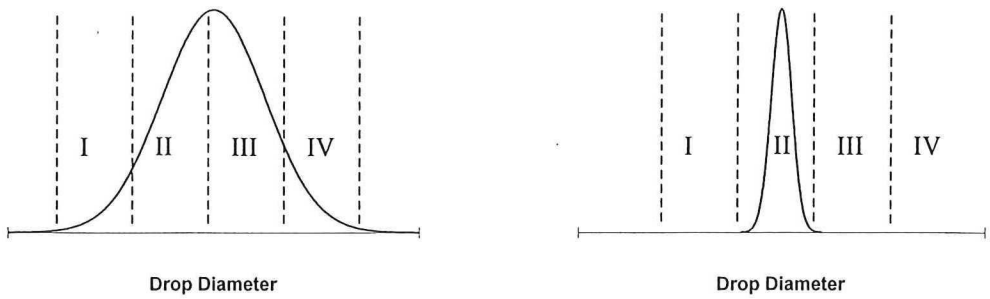

Figure 1.3 Illustration of the distribution compared with the industrial grades. On the left an example of an actual distribution. Right an ideal distribution.

Shell Research started a project to determine how to narrow bead size distributions of expandable polystyrene. Because experimenting with industrial vessels is far too expensive, small scale stirred vessels are used in this research. The consequence is that process conditions are different: a recipe for a batch of narrow EPS in a laboratory scale vessel can not be applied straightforwardly to the industrial scale.

The main question is: how do we implement the recipes for the industrial scale reactors? What, for instance, has to be the stirrer speed to gain the same kind of dispersion. In other words, what are the scaling rules? This project aims at solving the specific problem of scale-up.

With these scaling-rules it is possible to predict bead size distributions of polystyrene in industrial scale plants. New recipes can be implemented in an analytical way instead of using an expensive trial and error approach. The costs of EPS production are thus considerably reduced. Only the hydrodynamic aspects of the process are taken into account in this project.

Experiments are conducted on three vessel scales. Dispersions were made in these vessels. The drop size density was measured for different conditions. A new measurement system is developed for this task as no satisfactory drop size measurement system existed.

In chapter 2 the theory of dispersions and scaling rules is given. Chapter 3 reports on the conducted experiments. In chapter 4 the developed drop size measurement system is described. In chapter 5 it is described how big the sample must be to produce a reliable drop size distribution. Chapter 6 presents and discusses the measurement results and in chapter 7 the conclusions are given as well as the recommendations.

2 Theory

2.1 Vessel and impeller characteristics

In stirred vessels mixing is accomplished by a rotating impeller, which establishes a flow pattern in the vessel. Next to generating a mean flow, the impeller induces turbulence. Turbulent mixing is much more effective than laminar mixing, because the fluctuations and structures enlarge the contacting area between reactants in the vessel. In this research no reactants are used but immiscible fluids. When a vessel containing two immiscible liquids is agitated, a dispersion is formed in which continuously break-up and coalescence of drops occurs. Eventually a dynamic equilibrium is established for which the average drop size and drop size distributions depend on physical properties and conditions of agitation.

There are various types of vessel geometries and impellers. Most vessels are cylindrical with a diameter about equal to their height. Vessels can be curve-bottomed or flat-bottomed. In industry vessels are often curve-bottomed. In research however, almost every vessel investigated is flat-bottomed. Also in this project flat-bottomed mixing vessels were used. They have the advantage that a lot of literature is available on the flow in such vessels and that the implementation in a computer code is straightforward. Further, it seems plausible that results of investigations concerning scaling in flat-bottomed geometries can be applied to curve-bottomed vessels as well

Impellers are available in various kinds, see Fig 2.1 Two frequently used types are the pitched blade turbine and the disc turbine. The first pumps fluid axially, while the latter induces a radial flow, leading to two circular loops, one under, one above the impeller, see Fig 2.2. Of course, both impellers bring about a tangential flow as well. This tangential flow is usually hindered by four baffles inserted at the circumference of the vessel. Due to baffles more turbulence is created, leading to a higher mixing quality of the vessel.

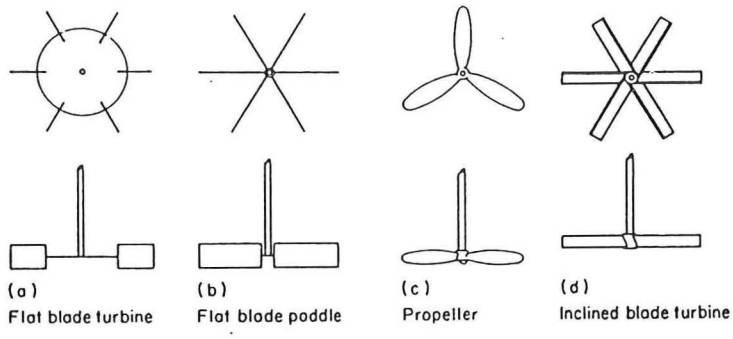

Figure 2.1 Various types of impellers [1].

In this project a pitched blade turbine is used. Its rotational direction is such that it pumps liquid axially downwards. In this way particles can be kept better in suspension, e.g. in a suspension polymerisation process. More research is done on standard disc turbines. It is believed however that results with respect to scaling obtained with a disc turbine are equally applicable to inclined blade impellers and vice versa.

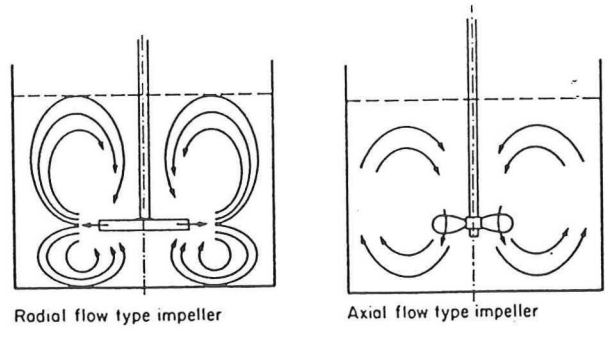

Figure 2.2 Flow patterns of impellers [1].

2.2 Characteristics of the flow

For the interpretation of the experimental results it is necessary to know the hydrodynamic conditions in the vessels. The flow must be at least turbulent to obtain complete dispersion. The transition from laminar to fully turbulent flow takes place over a fairly large range of the Reynolds number, Re, see equation (2.1). The Re number can be interpreted as the ratio of the momentum transport by convection ($\sim\rho v^2$) and the momentum transport by diffusion ($\sim\eta v/D_c$). Where ρ is the density of the fluid, v the characteristic velocity, η the dynamic viscosity and D_c the characteristic length scale. Fully turbulent flow is obtained when $Re > 10^4$. For flows in stirred vessels Re is:

$$Re = \frac{\rho N D^2}{\eta} \tag{2.1}$$

with rotational impeller speed N and impeller diameter D.

The Froude number characterises the amount of vortexing or gas entrainment in a tank that has a free surface. This is when impellers draw down gases from the surface. The Froude number, Fr, can be interpreted as the ratio of inertia forces and gravity forces.

$$Fr = \frac{N^2 D}{g} \tag{2.2}$$

Where g is the gravitational acceleration. The Power number Po characterises, from the energy point of view, the power input into the vessel. The equation for the power number is:

$$Po = \frac{P}{\rho N^3 D^5} \tag{2.3}$$

Where P is the power input. By dimensional analysis it has been demonstrated, that the power required for agitating a vessel, is dependent on the Reynolds number, the Froude number and geometrical ratios. As stated earlier, in this project geometrically similar baffled vessels were used. Also stirrer speeds were kept low enough to avoid gas entrainment. Therefore, the latter two factors can be left out. What is left over, is a relation between power number and Reynolds number. This can be demonstrated as follows:

During agitation, impeller blades experience a drag force which can be characterised by a drag coefficient:

$$C_d = \frac{F}{\frac{1}{2}\rho v^2 A_b} \tag{2.4}$$

where F is the drag force, v and A_b a characteristic surface, proportional to the area of the impeller blades. The drag coefficient only depends on the Reynolds number. Now, keeping in mind that the agitation power is the product of drag force and characteristic velocity, and with v~ND and A_b~D^2, the following relation can be derived:

$$Po = \frac{P}{\rho N^3 D^5} = f(Re) \tag{2.5}$$

where Po is the Power number. The power number, from a forces point of view, can thus be interpreted as a drag coefficient. The relation between Po and Re is different for each stirred vessel geometry. This is demonstrated in Figure 3.3 where some power curves are depicted for a single phase flow.

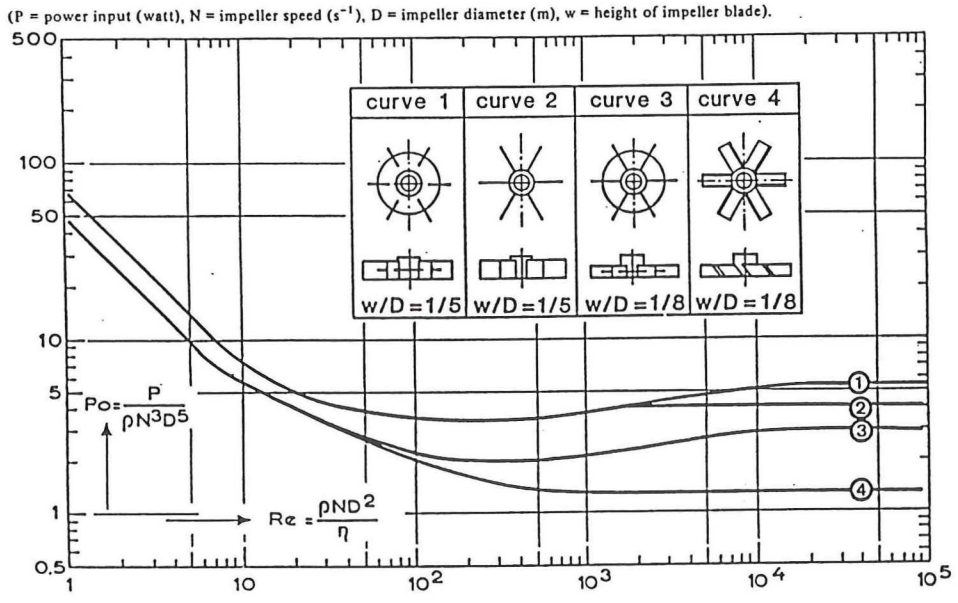

Figure 2.3 Power curves for different impellers [9].

The different values for Re:

- Re < 10: The flow can be characterised as laminar. In this region the Power number, or drag coefficient C_D is inversely proportional to the Reynolds number, as can be seen in the double logarithmic plot.
- 10 < Re < 10000: The flow is in a transition regime, and with increasing Reynolds number more and more turbulence is generated. From Figure 3.3 it can be seen that the Power number in the transitional regime does not differ much from the fully turbulent regime.
- Re > 10000: The flow is fully turbulent and the Power number is constant.

The mean energy dissipation per unit mass is described with equation (2.6):

$$\bar{\varepsilon} = \frac{P}{\rho V} = \frac{4 Po N^3 D^5}{\pi T^2 H_l} \tag{2.6}$$

Where T is the tank diameter, H_l is the liquid height in the tank and V is the liquid volume in the tank. With $T \sim D$ and $H_l \sim D$ the scaling rule for constant specific power input would be:

$$\bar{\varepsilon} = C_1 N^3 D^2 \quad \text{or} \quad N^3 D^2 = C_2 \tag{2.7}$$

2.3 Liquid-Liquid Dispersions

2.3.1 minimum stirrer speed for dispersions

When a liquid-liquid dispersion is being made, it has to be kept in mind that below a certain stirrer speed no complete dispersion will be obtained. The term 'complete dispersion' is used for a situation in which no large drops or agglomerates of droplets are found on the bottom of the vessel or at the liquid surface. In order to obtain 'complete dispersion', small-scale turbulent structures will play an important role. The velocity at this scale has to be sufficiently high compared with the rise or settling velocity of the droplets.

This was investigated by Nagata [13], and he concluded that for scale-up the power input per unit mass had to be kept constant in order to keep complete dispersion.

Van Heuven et al [8], also investigated the minimal agitator speed for dispersions, and they concluded that for scale-up $N^{2.6} D^3$ has to be kept constant. They concluded that minimum stirrer speed is not determined by small-scale flow only, but that there is some influence of larger scale flow on this process.

2.3.2 Time scales for a dispersion

It is generally assumed that dispersions are controlled by two processes. Break-up and coalescence. The mean drop diameter will be constant in time if the impeller speed is kept constant. There is in that case an equilibrium of the two effects. Nishikawa et al [15] examined the time to reach an equilibrium situation after a change of impeller speed. They found that the time to reach equilibrium is much longer if the equilibrium state is approached coming from high impeller speeds (i.e. with help of the coalescence process) than if the equilibrium state is approached coming from low impeller speeds (i.e. with help of the break-up process). This is illustrated in Fig 2.4 for a low fraction dispersed phase

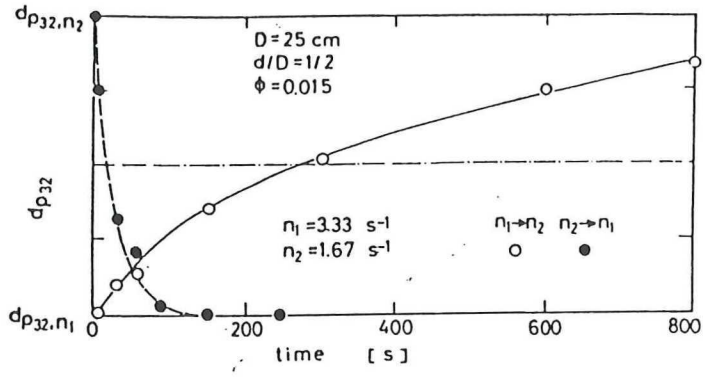

Figure 2.4 Change of drop size with time after change of impeller speed [15].

In Figure 2.4 ϕ is the volumetric fraction of dispersed phase. n_1 and n_2 are the impeller rotational speed only and d_{p32} is the mean sauter diameter (see equation 2.8.)

2.3.3 The shape of the drop size distributions

Different shapes are found in literature for equilibrium drop size distributions. Godfrey et al [6] found a normal number distribution, with dispersed phase hold-ups between 0.03 and 0.5, ($0.03 < \phi < 0.75$).

Calabrese [3] found for a low fraction dispersed phase ($\phi \leq 0.0015$) and a drops with low viscosity (0.1 to 0.5 Pa s) a normal number distribution. And for dispersions with drops with higher viscosity (5 to 10 PA s) and the same fraction dispersed phase, a log normal distribution.

Okufl et al [17] found a normal volume distribution. The hold-up fractions ranged from 0.1 to 0.4. And using n-heptane with a viscosity of 0.4 pa s.

Brown et al [6] found a bimodal volume distribution especially for the higher fraction dispersions. They experimented with volume fractions of 0.05, 0.1 and 0.2, the dispersed phase viscosity was 1.62 cP. Two possible explanations are given for finding a bimodal distribution in the article:

- The first explanation is reported earlier by Ward and Knudsen [26], and they suggested that this bimodal form arose from a combination of break-up and coalescence mechanisms being superimposed.

- Brown et al [2] conclude that if no coalescence is occurring in the system then all the drops have been generated by the break-up process. A complete disruption of large drops into several small ones would presumably be a random process and result in a normal distribution. Thus the production of a bimodal distribution arising from only a break-up process must be due to the fact that this process is an orderly removal of small elements from drops whose sizes are approaching the maximum stable value. Thus two super-imposed normal distributions arise with one mode representing the maximum stable drop size and the other characteristic of the typical sized drops which can be removed by the turbulence from drops approaching the equilibrium size.

2.3.4 Drop size correlations described in literature

The experimental investigations in the field of dispersions are usually occupied with the determination of the mean or Sauter diameters, or with the determination of the interfacial area per unit volume. The Sauter mean diameter is defined by the relationship:

$$d_{32} = \frac{\sum d^3}{\sum d^2} \tag{2.8}$$

and the surface area per unit volume by the next equation:

$$a_i = \frac{6\phi}{d_{32}} \tag{2.9}$$

Where d is a drop diameter, d_{32} the Sauter mean diameter and ϕ the volumetric fraction of dispersed phase. Although the Sauter mean diameter does not give any information on the width of a distribution, it can be used to evaluate the experiment that will be described in this report with similar experiments in literature. The parameters that will be used to describe a distribution are explained in section 2.4.

Godfrey et al [6] investigated Sauter mean diameters of liquid droplets in pumping devices. They arrived at the following empirical equation:

$$\frac{d_{32}}{D} = C_3\left(1 + C_4\phi\right)We^{-0.6} \tag{2.10}$$

Where D is the impeller diameter, ϕ and We is the impeller Weber number given by:

$$We = \frac{N^2 D^3 \rho}{\sigma_i} \tag{2.11}$$

Where σ_i is the surface tension. A large number of investigators found similar relationships. An overview of this literature is also given in [6].

Nishikawa et al [14] concluded that the contribution of middle-scale turbulent eddies to the energy spectrum of turbulence increases when scale-up of mixing vessels is done. This while keeping $\bar{\varepsilon}$ constant for geometrical similar vessel. The contribution of smaller eddies is preserved

notwithstanding the scale change. This observation implies that smaller drop sizes are obtained for larger-scale vessels when $\bar{\varepsilon}$ is used as the scale-up standard. Assuming that the turbulent fluctuations of middle-scale eddies, whose scale is from 100μ to a few mm in ordinary cases, controls the break-up phenomena.

Nishikawa et al [16] distinguish two correlation's. One particular for the break-up region ($\bar{\varepsilon}$ typically $0.05 m^2/s^3$):

$$\frac{d_{32}}{D} = C_5 \left(\frac{T}{T_0}\right)^{-\frac{2}{5}} \left(1 + 2.5\left(\frac{T}{T_0}\right)^{\frac{1}{2}} \phi^{\frac{2}{3}}\right) We^{-\frac{3}{5}} \tag{2.12}$$

And one for the coalescence region ($\bar{\varepsilon}$ typically 2.5 m^2/s^3).

$$\frac{d_{32}}{D} = C_6 D^{-\frac{3}{8}} \left(\frac{T}{T_0}\right)^{-\frac{1}{4}} \left(1 + 3.5\left(\frac{T}{T_0}\right)^{\frac{1}{2}} \phi^{\frac{3}{4}}\right) We^{-\frac{3}{8}} \tag{2.13}$$

Where T is the tank diameter, T_0 is the reference tank diameter, a constant value for different scales. The viscosity terms are left out as these terms are constant in this research. The correlative equation for the break-up region (2.12) is dimensionless, though that for the coalescence region is not because of the term $D^{-3/8}$ on the right hand side of equation (2.13). This is because the authors do not take in account the full physics in their study.

Nishikawa et al [16] also determine $\bar{\varepsilon}_{cr}$ and We_{cr} whose values show the transitional point of dominant process of drop formation.

The same authors found a correlation for the maximum drop diameter in a dispersion. In the coalescence region $d_{max} = 2.2 d_{32}$ and for the break-up region $d_{max} = 2.0 d_{32}$.

2.4 Drop size distributions

There are four types of drop size density functions: volume-, surface-, length- and number-density function. Traditionally when working with particles like EPS, the volume density function $f_v(d)$ is used to describe the distribution. This is mainly because it is easy to measure: a sample of particles is sieved and the weight of the different fractions is proportional to the volume of the fraction. A number distribution $f_n(d)$ in this example would be if all the particles of a fraction are counted. The volume distribution is characterised with the parameters d_{84}, d_{50}, d_{16}. The parameter d_p is defined as:

$$100 \frac{\int_{d_p}^{\infty} f_v(d)d(d)}{\int_{0}^{\infty} f_v(d)d(d)} = p \qquad \text{with } p = 16, 50, 84 \qquad (2.14)$$

In equation (2.14) d is the diameter of a particle, $f_v(d)$ is the drop size volume density function. d_p can be interpreted as the drop diameter for which p% of the total volume in drops has bigger diameters. These parameters are shown in Figure 2.5 for a normal volume drop size density function (A). And for the corresponding cumulative drop size density function $f_c(d)$ in (B). The cumulative drop size density function is defined as:

$$f_c(d) = 100 \frac{\int_{0}^{d} f_v(d)d(d)}{\int_{0}^{\infty} f_v(d)d(d)} \qquad (2.15)$$

As a result of these definitions $f_c(d_{84}) = 16$; $f_c(d_{50}) = 50$; $f_c(d_{16}) = 84$.

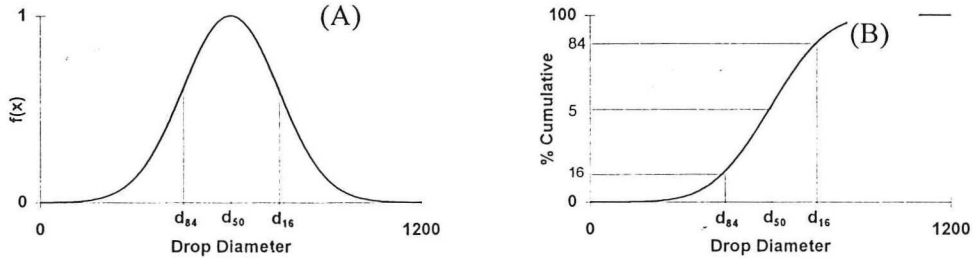

Figure 2.5 The volume drop size density function (A) and the corresponding cumulative drop size density function (B) with the characteristic parameters d_p. Diameters in μm.

If we assume that the drops are normally distributed in volume the drop size density $f_v(d)$ can be described with the following function:

$$f_v(d) = \frac{e^{\left(-\frac{(d-\mu_d)^2}{2\sigma_d^2}\right)}}{\sigma_d \sqrt{2\pi}} \qquad (2.16)$$

With μ_d the average drop size of the distribution and σ_d the standard deviation of the normal distribution.

The integral of $f_v(d)$ equals 1:

$$\int_0^{\infty} \frac{e^{\left(-\frac{(d-\mu_d)^2}{2\sigma_d^2}\right)}}{\sigma_d\sqrt{2\pi}}\,d(d) = 1 \qquad (2.17)$$

The lower boundary of equation (2.17) is taken 0 as no negative drop diameters exist. In the case of a normal distribution the d_{50}-d_{84} and d_{16}-d_{50} are equal to the standard deviation σ_d. In Figure 2.5 μ_d is 600 μm and σ_d is 150 μm. With the d_{50}-d_{84} and d_{16}-d_{50} parameters it is possible to see if the distribution is asymmetric and to determine the width of the distribution.

The drop size measurement method that is used in the experiments (chapter 5) will give a number distribution. From the volume density function we can derive a number density function. To obtain an integral of 1 again, the function has to be divided by its total surface.

$$f_n(d) = \frac{f_v(d)}{d^3 \int_0^{\infty} \frac{f_v(d)}{d^3}\,d(d)} \qquad (2.18)$$

The number density function of a normal volume density function is:

$$f_n(d) = \frac{e^{\left(-\frac{(d-\mu_d)^2}{2\sigma_d^2}\right)}}{d^3\sigma_d\sqrt{2\pi}\int_0^{\infty} \frac{e^{\left(-\frac{(d-\mu_d)^2}{2\sigma_d^2}\right)}}{d^3\sigma_d\sqrt{2\pi}}\,d(d)} \qquad (2.19)$$

It is evident that according to equation (2.19) at d=0 there is an infinite number of particles. This is illustrated in Figure 2.6, for two different density functions.

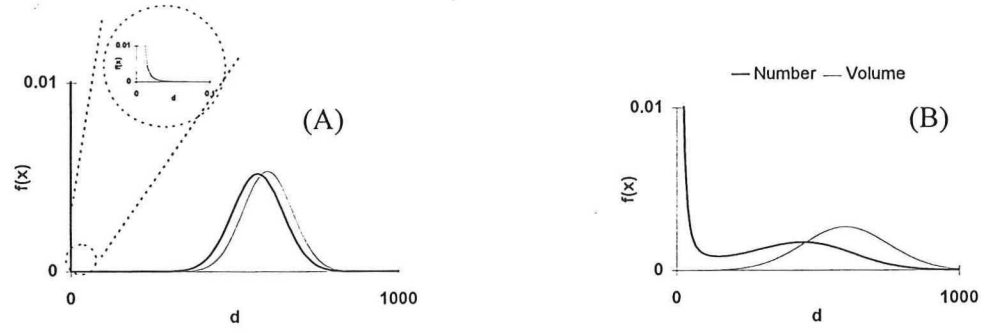

Figure 2.6. Number distribution together with its corresponding volume distribution. (A):μ_d is 600 μm and σ_d 75 μm. (B) μ_d is 600 μm and σ_d is 150μm. d is in μm.

In Figure 2.6 is drawn a volume distribution together with its corresponding number density function. The difference is not big in (A), the number distribution is shifted a little to the left. In (B) the distribution is wider than (A).

3 Experimental set-up

3.1 Introduction

In this chapter the experimental conditions for measuring the dispersions in the different vessels is described. The aim of the design of the experiments is to acquire a maximum of information out of a minimum number of experiments. The drop size distribution of a dispersion is a function of many parameters. We are primarily interested in scaling rules of dispersions. Therefor only the sizes of the vessels is varied. The experiments are designed in such a way that as many parameters as possible are kept constant, varying only one parameter at the time. In this case, the vessel geometry was kept constant and the ratio of the diameters between two vessels is constant. The power input was kept constant for the different scales. Dimensionless mixing times were constant, also the addition of surfactants was kept constant.

3.2 Mixing vessels, size, geometry

Experiments have been performed on pilot-scale in geometrically identical perspex vessels of 133.4 litre, 14.7 litre and 1.8 litre. (diameters: 48 cm, 23 cm and 11.4 cm). The flat-bottomed vessels were all half filled (in height) with de-mineralised water and for the other half with silicone oil (see section 3.3). The vessels were all equipped with three pitch-blade turbines (with four blades per impeller) and four baffles. Vessel and impeller are depicted in Figure 3.1. In the large vessel a 1.7 kW stirrer motor from EKATO with a variable rotational speed was used. Its number of revolutions was variable from 0 to 900 RPM. In both the medium vessel as well as in the small vessel a JANKE&KUNKEL 20 DZM stirrer motor, adjustable from 60 to 2000 RPM, was used. The dimensions of all three set-ups as defined in Figures 3.1 can be found in Table 3.1.

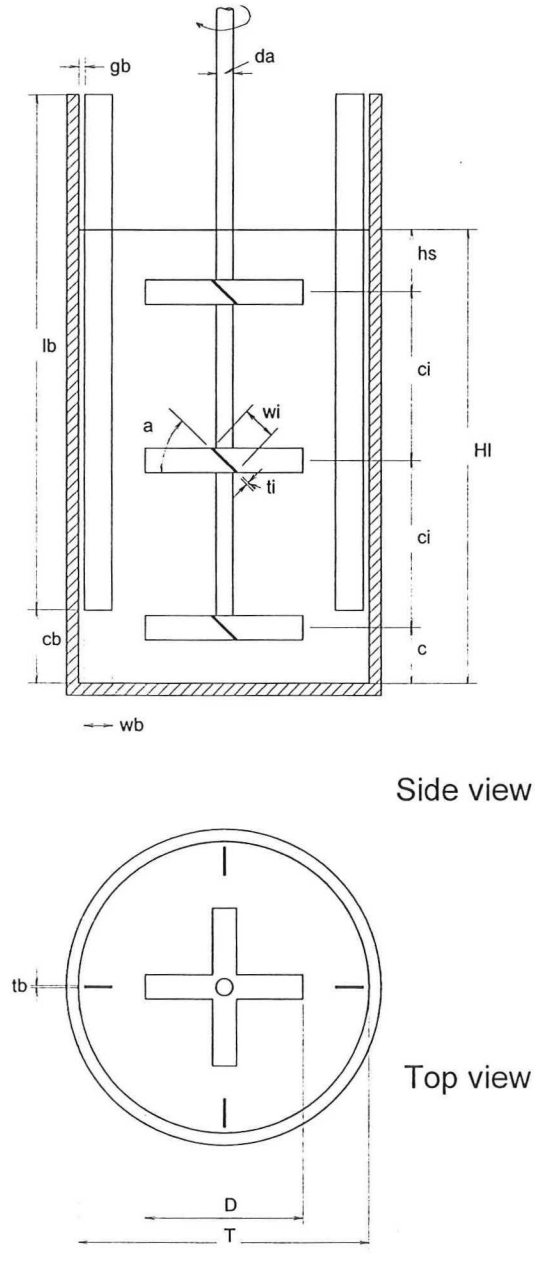

Figure 3.1. Drawing of the vessel used in the experiments.

		small	medium	large
a	Impeller angle	45°	45°	45°
c	Clear bottom	22	44	91
c_b	Clear Baffle	29	58	120
c_i	Distance impeller	65	132	275
D	Impeller diameter	62	124	260
d_a	Diameter axis	7	13	27
g_b	Baffle gap	2	5	10
H_I	Liquid height	175	353	737
h_s	Submerge impeller	23	46	97
l_b	Baffle length	199	402	840
T	Diam. react.	114	230	480
t_b	Baffle thickness	0.7	1.5	3
t_i	Impeller thickness	0.7	1.5	3
V_I	Liquid volume	1.8	14.7	133.4
w_b	baffle width	11	22	46
w_i	impeller width	13	26	55

Table 3.1. Dimensions of the vessels used in the experiments (in mm).

3.3 Choice of liquids

The aim of the project was to determine the drop size distributions of water and styrene. In the current laboratory set-up it was impossible to do experiments with styrene for a number of reasons. Styrene deteriorates the perspex vessels by creating hairline cracks. The vapour of styrene is toxic. The flash point is at 31 °C which makes it explosive. An alternative must be selected for styrene. In literature the following combinations of liquids are found for experiments concerning the mixing of immiscible fluids.

disperse phase	**continuos phase**	**authors**	**ref.**
n-heptane	water	Okufi, Perez de Ortiz & Sawistowski	[17
n-heptane+ DEHPA	water	Okufi, Perez de Ortiz & Sawistowski	[17]
honeybees wax	water + o-xylene	Nishikawa, More, Fujieda & Kayama	[16]
carbon tetracloride	water + Na_3Po_4	Konno, Aoki & Siato	[10]
carbontetrachloride	water	Mersmann &Grossman	[11]
Dichloride	water	Mersmann &Grossman	[11]
2-ethylhexanol	water	Godfrey, Obi & Reeve	[6]
Cumene	water	Godfrey, Obi & Reeve	[6]
silicone oils	water	Calabrese, Chang & Dang	[3]
styrene + PVA	water	Chatzi, Boutris& Kiparissides	[4]
toluene	water	YI & Tavlarides	[27]
styrene	water	Tanaka, Hosogai	[23]

Table 3.2. Combinations of disperse and continuos phase used for investigation dispersions.

The most important property of styrene to match when searching for an alternative, is the density. This has to be smaller than the continuos phase, water. Secondly the viscosity and the surface tension have to match. It was chosen to use silicone oils, (dimethylpolysiloxane), as the disperse phase. It is possible to adjust the viscosity of these silicone oils by mixing silicone oils with different viscosity's. As the flash point of some low-viscosity oils are below room temperature, mixtures with these oils are unstable because the low viscosity fractions will evaporate. The silicone oil used in the experiments was made by Rhône poulenc (type 47 V 5) and had according to the specifications a viscosity of 5 mPa s. This is five times higher then the viscosity of styrene. See table 3.3.

continue phase			de-mineralised water	styrene	Silicone oil
density-	ρ	Kg/m^3	996.29	904.18	920(*)
viscosity	η	mPa s	1.02	0.754	5(*)
surf. tens. (with air)	τ	mN/m	70 (*)	31.12	19.7(*)

Table 3.3. Properties of the different liquids used for the experiments. All at 20° (except for (*): at 25°)

3.4 Scale experiments

The conditions of the experiments must resemble the industrial conditions. First of all the dispersion has to be turbulent. This means that the Reynolds number (equation 3.1) has to be sufficiently large; $Re > 1.10^4$.

$$Re = \frac{\rho N D^2}{\eta} \tag{3.1}$$

Here N is the stirrer speed in rotations per second, D is the stirrer diameter and ρ is the density in kg/m^3. Secondly the vortexing of the vessel has to be minimised. Vortexing is the dispersion of gas in the vessel, sucked in from the surface by a vortex. The Froude number (equation 3.2) characterises this phenomenon. It showed that if $Fr > 0.08$ occasionally swarms of air drops showed in the vessel. And it was observed that if $Fr > 0.3$, air bubbles were homogeneously dispersed over the vessel.

$$Fr = \frac{N^2 D}{g} \tag{3.2}$$

The speed of the stirrer is scaled on basis of equal energy dissipation per mass. This is given by the next formula:

$$\bar{\varepsilon} = \frac{P}{\rho V} \tag{3.3}$$

Where $\bar{\varepsilon}$ is average energy dissipation in W/kg. P is the power input in W, and V is the volume in m^3. The average energy dissipation is calculated with the following equation

$$\bar{\varepsilon} = \frac{Po\, N^3 D^5}{V} \tag{3.4}$$

This means that Po can be determined if the power input is known. For this a power measurement is done: At a certain stirrer speed N the torque is measured. From the torque the power input can be calculated with:

$$P = 2\pi NM \tag{3.5}$$

Where M is the torque of the stirrer in Nm. In this way the final formula for Po becomes:

$$Po = \frac{2\pi M}{\rho N^2 D^5} \tag{3.6}$$

With error formula:

$$\left(\frac{\delta Po}{Po}\right)^2 = \left(\frac{\delta M}{M}\right)^2 + \left(\frac{\delta \rho}{\rho}\right)^2 + 4\left(\frac{\delta N}{N}\right)^2 + 25\left(\frac{\delta D}{D}\right)^2 \tag{3.7}$$

The values of the Po number are shown for different values of Re in the next figure along with error bars. A power measurement is also conducted on a one-phase system. From that experiments the Fr values for vortexing could be determined visually. In the two phase system for the density the average densities of both phases is used, while for the viscosity the continuous phase (water) viscosity is used.

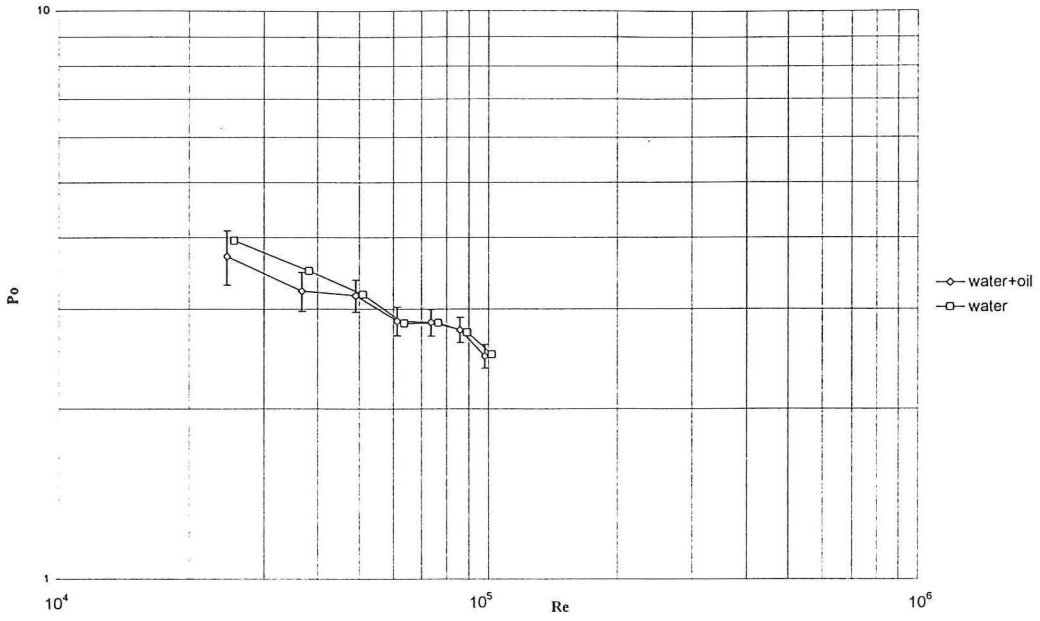

Figure 3.2. Power number vs. Reynolds number

Figure 3.2. shows that Po decreases with increasing Re. According with theory the Po should become constant. The value of Po is constant for Re ranging from 6.10^4 to $9\ 10^4$ For higher Re, Po continues to decrease. This is probably due to the observed entrainment.

The power experiment is conducted with the middle vessel and with a Ekato "Fluid" torque meter (absolute error is 500 Nm). In the chosen regime the Po number is 3.16 ± 0.21.

Now with equation (2.6) we can determine the rotational speed of the impeller for a given scale and specific power input.

It was chosen to do measurements with three different power inputs per vessel. Low, medium and high power input, (lo, mi, hi). The respective values are: 0.20, 0.25, 0.31 W/kg. The three different power inputs are depicted in the next chart along with the restrictions concerning the turbulence, Re, and Vortexing, Fr, for the three different scales. Also a typical industrial power input is showed, (in).

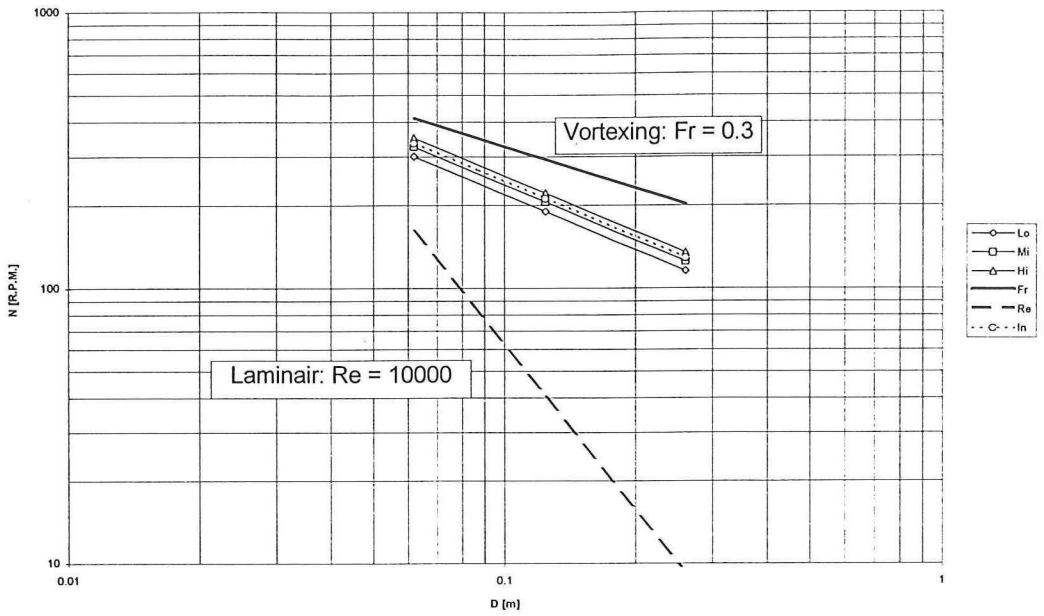

Figure 2.3. Scaling on basis of constant power input. Compared with industrial value. For each diameter is depicted the maximum and minimum possible rotation speed.

In each of the three vessels three experiments are done. First a measurement with low power input. Then after a fixed time Δt, a measurement with a medium power-input. Finally after Δt a measurement with high power input. In the next figure is a diagram of the measurement sequence.

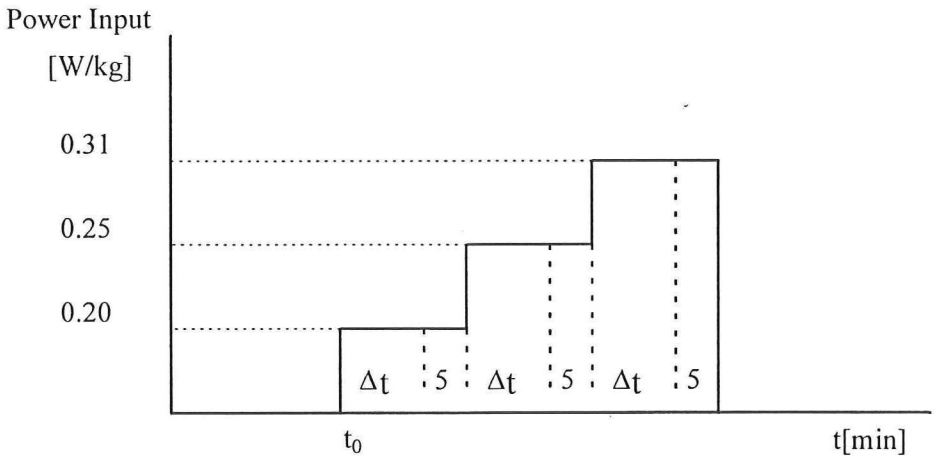

Figure 3.3. Measuring sequence of the dispersion in the stirred vessel.

The actual drop measurement took 5 minutes The time between the measurements Δt was scaled on basis of number of rotations:

$$N \cdot \Delta t = C_7 \tag{3.8}$$

With C_7 as a constant. In Table 3.3 the rotation speed for the stirrers in RPM along with the Δt in minutes are depicted .

		vessel		
		small	medium	large
Power Input	0.20	300	188	115
	0.25	325	204	125
	0.31	350	219	134
time before measuring	Δt	45	72	117

Table 3.4. RPM of the stirrer for three different vessels and three different power inputs. Δt [min] between measurements for the different vessels.

The place of measurement was between the baffles in the plane of the interface of the system at rest. The endoscope is pointed outwards of the vessel for external illumination. The distance from the wall is for the large medium and small vessel respectively: 10, 6 and 3 mm.

3.5 Surface activity

In the past many people have tried to work with pure two-phase systems. In time it became clear that small impurities have a big effect on the surface tension of the system and may trouble with the reproducibility of the experiment (personal communication with Agterof, Unilever research lab.). The surface tension has a big influence on the drop size and on the drop size distribution in a stirred vessel. To avoid the very difficult task of trying to keep the system pure, a small quantity of surface active material is added. The aim is to add just as much surfactants to overrule the impurities and at the same time to avoid that the surface active material controls the drop size distribution of the whole dispersion.

3.5.1 Theory of surfactants

The chosen surface active compound is dobanol (91-10), a Shell brand name. It consists of 10 carbon atoms and 10 ethylene oxide groups $CH_3(CH_2)_9$-$(CH_2CH_2O)_{10}H$. The two different groups have different properties. One group is polar, and the other group is a-polar. The polar end (EO group) wants to dissolve in water, while the a-polar end wants to dissolve in the oil phase. See Figure 3.5.

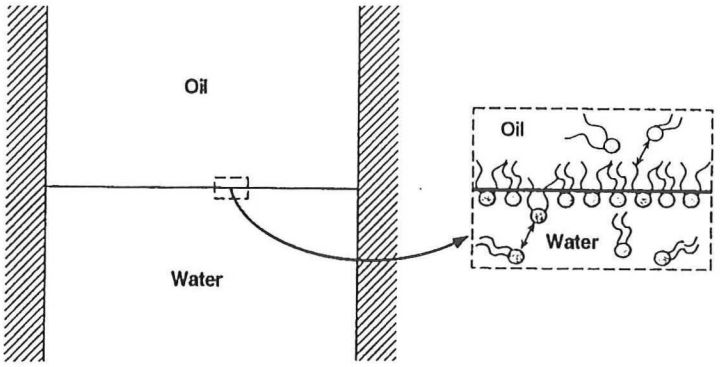

Figure 3.4. Macroscopic oil-water interface. Surfactants in the bulk phases are in dynamic equilibrium with molecules at the interface,[5]. The surfactant molecule in this illustration consists of two longer carbon groups.

As a result the surfactants tend to situate at the interface of oil and water. In the case of a drop of oil in water, the drop will be covered with surface active molecules. See Figure 3.6. By adding surfactants the surface active molecules will lie closer to each other. This continues until the distance between the molecules becomes so small that the repelling forces of the near surface active molecules are as big as the attraction forces of the interface. This saturation of the surface active material is called the critical micelle-concentration.

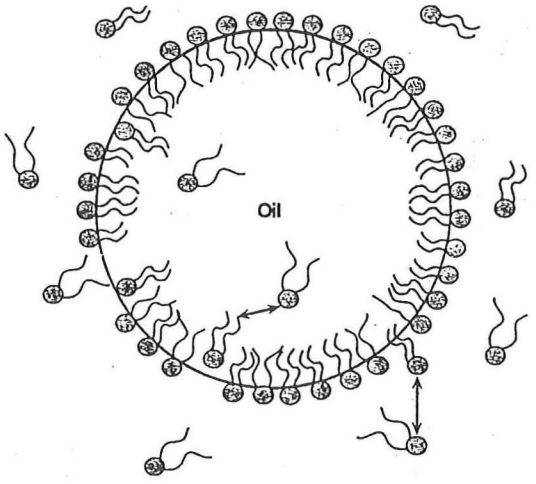

Figure 3.5. Surfactants are in a dynamic equilibrium between interface and bulk [5].

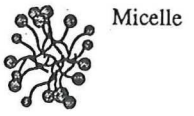

Figure 3.6. Micelle. [5]

Adding even more molecules will create independent cells of surface active molecules outside the interface. These are called micelles, see Figure 3.7.

The surfactants have an effect on the dispersion:

- With the surfactants the surface tension of the interface is lower. As a result, the turbulent flow can break up the drops further into smaller drops than without surfactants.

- The addition of surfactants also alters the coalescence rate. This is due to the non-uniformity of the surfactant interfacial density. Non-uniformity in this density induces Marangoni surface-driven flows, promoting formation of a stabilising surfactant film, [5]. Reducing in less coalescence.

- The different lengths of the groups and the ratio between these groups can have an effect on the dispersion:

- If the EO group is short compared to the carbon group, the surfactant tends to dissolve better in the dispersed phase (silicone oil). Then the mobility of the surfactant will be much lower than if the surfactant is dissolved in the continuos phase.

- A different length of the groups can alter the curvature of the surfaces. This is due to repelling forces of the surfactants between the same groups of different molecules nearby. See Figure 3.8.

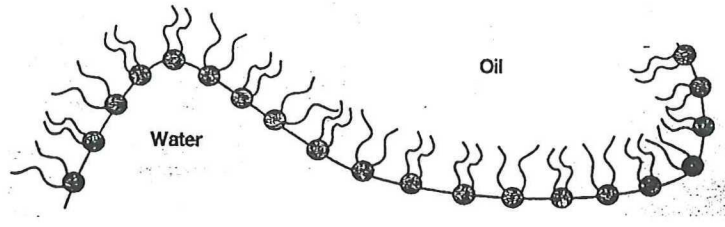

Figure 3.7. Perpendicular cut through an oil-water interface showing the curved surfactant film. Note the tighter chain packing when the film curves towards the oil compared to when it curves toward water. In the figures a surfactant molecule is drawn with two long carbon groups and a short EO group.

With the dobanol (91-10) the polar and non polar groups keep each other in balance. Ten EO groups and ten carbon groups.

3.5.2 Concentration

It was concluded by Agterof that the best concentration of surfactants was the critical micelle concentration. An experiment in the small vessel showed that this concentration was far too high for our purpose. The drops become very small, and were significantly altered by the surfactants. After switching the impeller off, the dispersion in the vessel did not separate due to gravity at all.

Another concentration had to be used. To find this concentration, some experiments were done in the small vessel. A solution was made of the dobanol and drops of the solution are added little by little in the vessel. The drops are made by a gas chromatography syringe. Video images were made of the dispersion. By comparing typical pictures of the video images a particular concentration was chosen. The pictures of the dispersion with the concentration that was chosen did not differ significantly with the pictures of a dispersion without any surfactant. A higher concentration of surfactants resulted in a dispersion with a less wide distribution and smaller average diameter of the drops The added surfactant dobanol used in the scale experiments is showed in table 3.5.

	dobanol [mgr.]
small	3.24
medium	26.60
large	241.85

Table 3.5. The added surfactant [mgr.] per vessel.

3.6 Signal processing

The output file of the drop size measurement method consists of a set of drop diameters. From these diameters the cumulative volume distribution and the parameters d_p (see section 2.4) were calculated. The diameters of the drops are not continuous but discrete. The classes or bins are equivalent to the resolution of the measurement method. A class with drops of diameter d_j [μm], (with $d_j < d_{j+1}$), has a class width c_w [μm] and contains n_j particles with a diameter between d_j - ½ c_w μm and d_j + ½ c_w μm. This results in $f_n(d_j) = n_j$. In order to calculate the characteristic parameters d_p, the number distribution first had to be transformed to the volume distribution:

$$f_v(d_j) = \frac{f_n(d_j) \cdot d_j^3}{\sum_{m=1}^{q} f_n(d_m) \cdot d_m^3} \tag{3.9}$$

In the formula q is the number of bins. $f_v(d)$ is scaled such a way that it's sum equals 1. The cumulative volume distribution in percentage (%) can be calculated from equation (3.9) by:

$$f_c\left(d_j + \frac{c_w}{2}\right) = 100 \cdot \sum_{m=1}^{j} f_v(d_m) \tag{3.10}$$

The values for d_p follow from equation (3.10). If $d_j < d_p \leq d_{j+1}$ .We find with a linear interpolation:

$$d_p = d_j + \frac{c_w}{2} + \frac{\left((100-p) - f_c\left(d_j + \frac{c_w}{2}\right)\right) \cdot c_w}{\left(f_c\left(d_{j+1} + \frac{c_w}{2}\right) - f_c\left(d_j + \frac{c_w}{2}\right)\right)} \tag{3.11}$$

The last equation will give the values for d_{16}, d_{50}, d_{84}, For p = {16, 50, 84}.

4 Drop Size Measurement

Many methods have been developed to measure drops in the chemical process industry. Some of the more popular methods used are reported in this chapter, along with the self developed method.

4.1 History

All the drop size measurement methods can be divided into two groups: intrusive and non intrusive. An intrusive method is a method where the system is altered by the measurement method. A few methods are described below.

Non intrusive:

In a transparent Laboratory set-up it is possible to make pictures or slides through the wall. From these images the various drop diameters can be deduced. With this method it is only possible to determine the drop size at the wall of the vessel, of a high concentration dispersed phase.

Intrusive:

Some fully developed methods already exist like the Lasentec Particle Sizer which is build for use in the process industry. It consists of a long metal probe that is inserted in the dispersion. It measures the chord of drops by means of two laser beams. The advantage of this method is that drop size distributions can be measured real-time. The disadvantage is that the measured raw data are transformed with help of statistical techniques to drop sizes. It is not clear what is measured: Is it an air bubble? is it constantly the same drop?

Another method is extracting a sample from the dispersion and then analysing it. This method is not only intrusive it also alters the total volume of the dispersion. To get a representative sample, the extraction must occur iso-kinetically. As a result, the behaviour of the flow must be known on the places where the extraction takes place. Just in front as well as in the extraction tube coalescence and break-up of the drop has to be avoided. This is generally done by adding surfactants to the sample or diluting the sample. One research project [16] recommends using hot beeswax as the dispersed phase. The wax solidifies when extracted into a cold environment and can not coalesce any more. The extracted sample can now be analysed in a number of ways. For example: with a capillary technique [19], with photography [8] or with a modified Fraunhofer technique [24].

4.2 Experimental set-up

The dispersion investigated in this project has a high (50%) fraction dispersed phase. It is only possible to take pictures from the vessel walls. This method does not satisfy our aim as we want to know the drop sizes at various positions inside the vessel. Due to the uncertainty of what happens

with an extracted sample, it was chosen not to use the extraction method. The Lasentec particle sizer has been tested at Shell [personal communication with Hans Visser (KSLA)] and does not give satisfactory results. As a result a completely new measurement technique was developed.

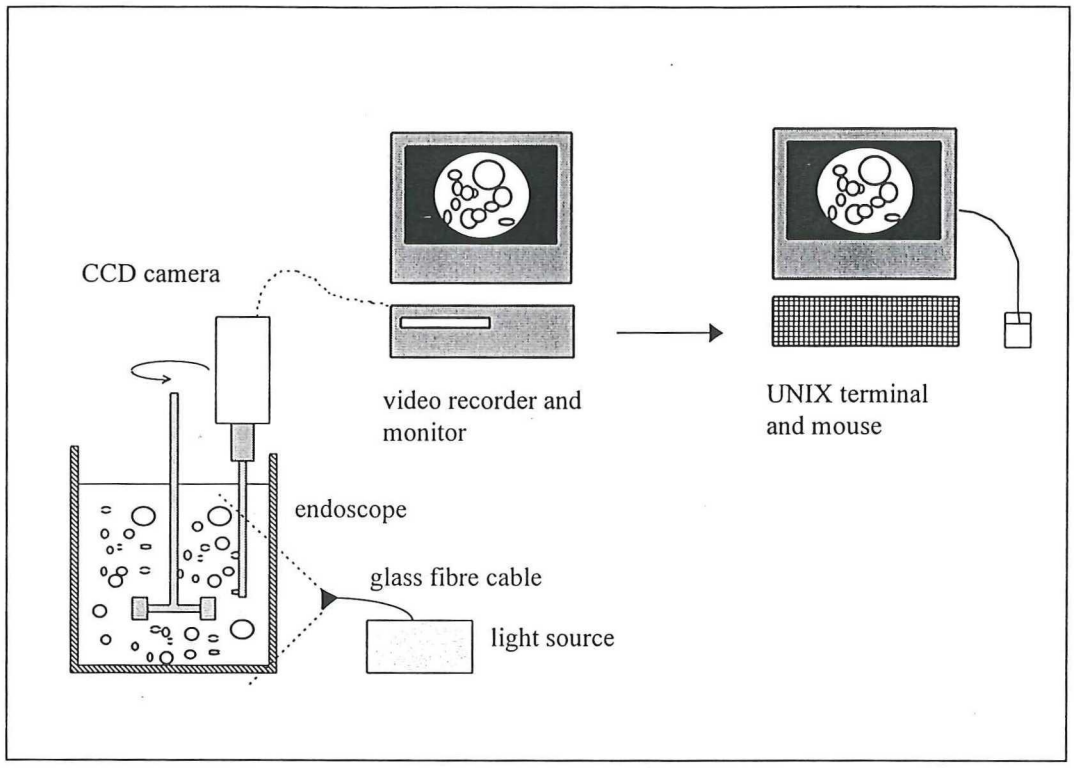

Figure 4.1 Experimental set-up for the endoscope video technique for drop size measurements

The developed Endoscope video technique Drop Size Measurement method (EDSM) (Figure 4.1) consists of a CCD camera mounted on an endoscope inserted in a stirred vessel that contains the dispersion. The images of the camera, illuminated by a light source, are taped by a video recorder. From the videotape the images are 'grabbed' and digitised by a PC. The PC sends them to a UNIX workstation where the images are analysed manually with help of an image processing tool. The EDSM enables detailed observation of the structure of a dispersion revealing the presence of droplets-in-drops and distinguishing air bubbles from liquid drops.

4.2.1 Endoscope

An endoscope is an optical device that makes it possible to look in small spaces under different angles with different magnification. Endoscopes are used for inspection purposes. For instance to inspect pipelines or for medical purposes. In this research two endoscopes were used. The dimensions of both endoscopes are similar. The first endoscope (endoscope1) is a HSW 90° Endolux optic. The second one an EFER BS 065 090 55 049 FR. The qualification 90° means that it monitors perpendicular to the endoscope. The angle of the field of view of both endoscopes is 60°. The distance of the focal plane was adjustable, (approx. 2 mm to ∞). The length of the intrusive part is 44 cm while the diameter is 4 mm for both endoscopes. Between the endoscope and the CCD camera an ocular was mounted. For endoscope1 the 0TV 35ES, and for endoscope 2 the ON 25 ES. This ocular coupled the

endoscope to the camera and focused the image on the camera. The adjustable ocular made it possible to slightly magnify the image.

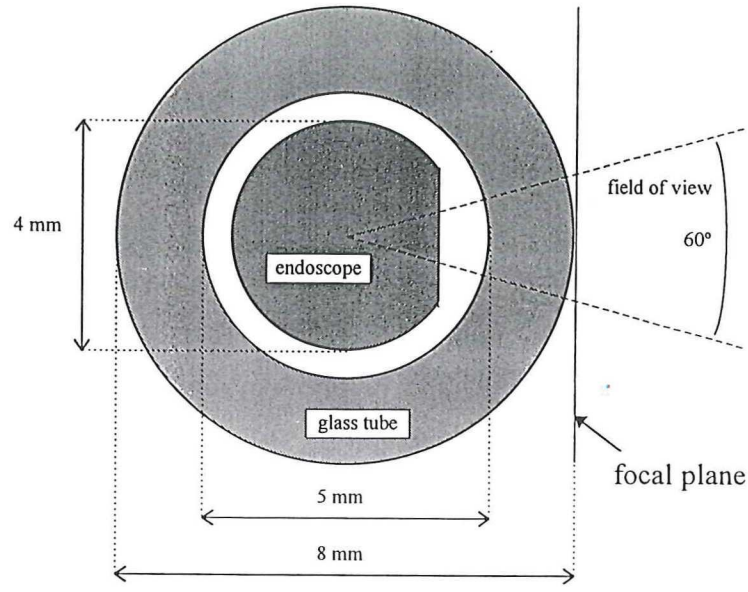

Figure 4.2 Top view cross section endoscope

A glass tube with inside diameter 5 mm and outside diameter 8 mm was fitted over the endoscopes, as shown in Figure 4.2. The tube was kept at a fixed distance by two Teflon spacers (inside diameter 4 mm outside diameter 5 mm). The tube had to be fitted because the adjustable focal plane of the standard endoscopel began at a particular distance from the outgoing window. This is done by the manufacturer to avoid that all the pollution and impurities on the window and lenses are seen. By inserting the endoscope in the glass tube the plane of focus coincides with the glass-liquid interface.

4.2.2 Camera

A Grundig FA-85 electronic high resolution camera was used. It consisted of a switchable shutter-function with 8 different electronic shutter times ranging from 1/60s to 1/10000s. The pixel resolution is 582(V)*762(H). The stirrer of the stirred vessel has a high tip speed (typically 1.5 m/s). This results in high liquid dispersion velocities. To get a sharp, frozen image the shutter time has to be small. In the experiments the shutter time was 1/10000 s. To get enough contrast on the CCD chip with these small shutter times, much light is needed.

4.2.3 Illumination

Not only a high intensity light source is essential, also its position is important. The standard endoscope consisted of an in-build light transmission to the area where the outgoing window is placed (see Figure 4.3). With this so-called backward scatter option it is possible to peek into tiny spaces. In

this mode the total amount of transmitted light proved to be insufficient for high shutter speeds. The contrast of the image with this mode was too small.

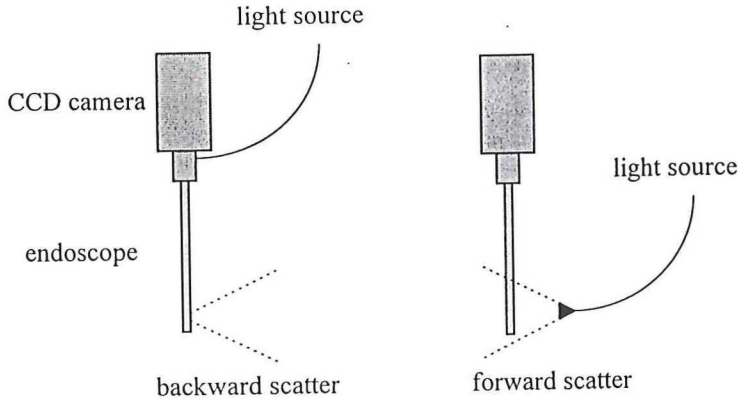

Figure 4.3 The two lighting modes

In all the experiments a forward scatter illumination was used, as this gave the best contrast. For the light source a Schot KL 1500 was used with a 15 V 150 W light bulb. The light is transported through a flexible waterproof glass fibre cable opposite to the endoscope. There it is emitted through a lens to focus the light. The disadvantage of using high intensity light is that the light locally heats up the dispersion.

4.2.4 Image acquisition

The images from the camera are directly taped on a Blaupunkt SVHS rtv 915 hifi video recorder. Because the PC that digitises the images was in another building, a second VCR (video cassette recorder) was used to playback the images. This VCR, a Blaupunkt ACT RTV 950, was linked to a Pentium PC with special Digital [21] soft- and hardware.

The PC grabs an image every second and digitises it in TGA format. This low frame sample speed results in a small chance that identical drops are measured more often. Also the total measurement time has to be much longer than the impeller-blade passage time, typically 50 ms. This to average out periodicity Bad images, underexposed, blurry or overexposed, are immediately manually rejected. The TGA-formatted images are then transported to a UNIX network where they are transformed to the TIF-format. The transformation does not alter the image, only its output format. This is the final format that can be handled by the image analysis software. The video resolution is 500 * 400 pixels. The grabbed images have a higher resolution than the video images, so no information is lost.

A video image consists of two separate images. These two (even and uneven) differ little in time and are merged into one. This is called interlacing. The PC grabs a complete images with a resolution of 500*400 pixels. Later the even image is separated from the uneven one as they differ slightly. The difference between even and uneven images result in a flickering still image. The final resolution of the TIF-format is therefore 500*200 pixels.

4.2.5 Image analysis

Fred Hoeve KSLA(MCA2) wrote the dedicated C-procedures for the scil-image software [22]. The program showed on command a picture sampled from the video tape. On such a picture the pixel radius of the drop is determined by clicking with the mouse on the circumference of the drop on three different places. The program will then draw a circle through the three points. The operator now chooses if the drop is accepted or rejected. If the drawn drop is not acceptable, because this circle doesn't fit the drop, then the circumference has to be pointed out again. Not all drops are acceptable. Before a drop is accepted a number of objective criteria had to be satisfied. This is very important because subjective choices give rise to different measurement results. And so duplication of experiments will not give a satisfactory result. The following criteria had to be met for a drop to be selected:

- First of all it has to be a dispersed phase drop and not an air bubble.
- The drop should be **completely** inside the mask.
- The majority of circumference has to be visible (roughly 80 % of the circumference).
- The drop has to be close to the lens.
- On every picture **all** the recognisable drops must be selected.

In fig (4.4) is an example of the computer screen with a picture of all the drops. The thick black circle is the mask that is put over the image. In fig (4.5) are depicted in grey the validated circles. In this particular case the smaller drops are in front of the bigger ones.

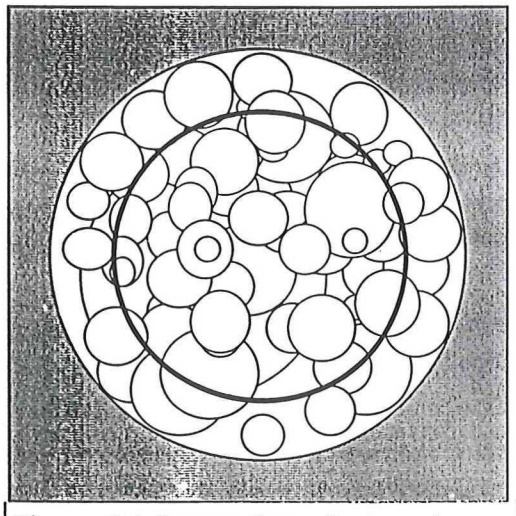

Figure 4.4 Impression of a raw image. The thick line represents the mask

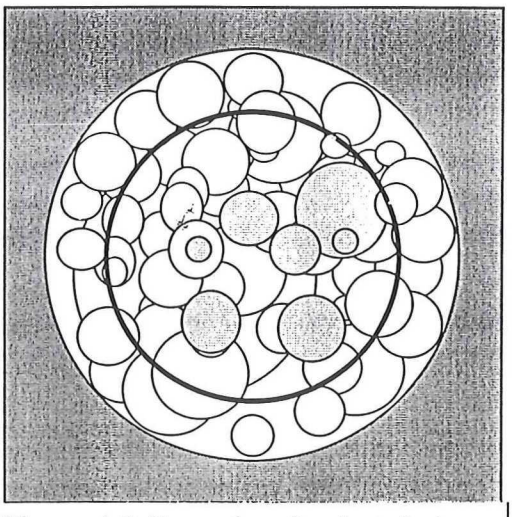

Figure 4.5 Example of selected drops. The thick line represents the mask

In some cases it is very difficult to determine the actual position of the drops. In fig (4.6) are examples of difficult determinable drops. In the example a projection in the 2-D plane results in four possibilities for the position of two drops in the 3-D plane. In the experiments the fluids were transparent.

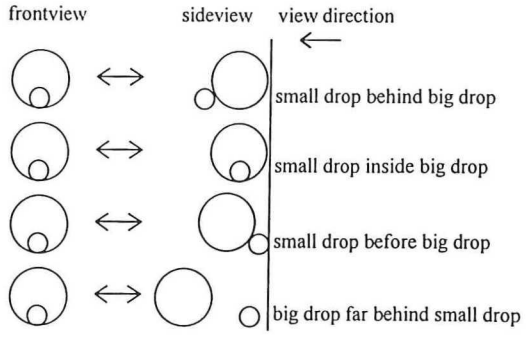

Figure 4.6 Different interpretations for two drops

The situations could be recognised the following way:

- In the first case the big drop is closest and validated. The smaller drop behind the big drop can be recognised because it is clearly optically deformed and seems elliptical.
- In the second case a drop of the continuous phase is inside the dispersed phase. The smaller drop tends to look bigger due to the magnification effect of the big drop. It is difficult to recognise this situation. If recognised neither of the drops are validated
- In the third case both drops should be validated as they are both close to the endoscope. The small drop does not optically deform the bigger drop. That is the main difference with the first case. In reality small drops tend to fill up the gaps between the big drops and the endoscope.
- In the fourth case only the small drop should be validated. The big drop looks smaller due to the perspective and may therefor not be selected. This case is rare with a 50% volume dispersion as there are always drops right in front of the endoscope.

In most cases with a good contrast, it is possible to see what the real situation is. The distant drops are optically deformed by the closer ones and will look elliptical. But this is not always the case, a good trained eye is needed to distinguish between the different cases. Because of this, it will be difficult to determine the drops automatically.

In the output file of the program the diameter of the drop and the co-ordinates of the centre of the drop are written (all in pixels). together with the image number of the particular drop.

4.3 Error estimation

Errors can be divided into two categories: objective and subjective. In this section all possible sources of error are listed.

4.3.1 Objective inaccuracy

Optical deformation by the glass tube

Because the glass of the tube around the endoscope is curved (Figure 4.7), all drops that originally are perfectly round will look slightly ellipsoidal.

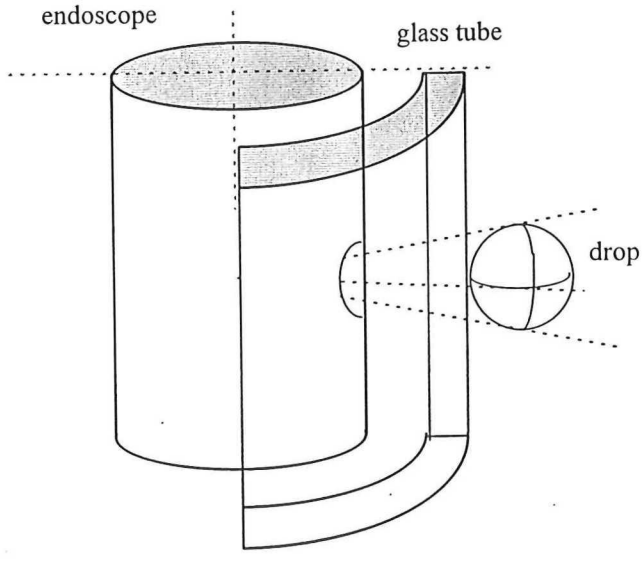

Figure 4.7 Cross section endoscope and glass tube

Optical deformation perspective

Drops more away from the centre of the image look smaller as the distance to the opening window is bigger. Even if drop rests against the glass tube. This is due to perspective.

Deformation by the endoscope

The image of the endoscope is deformed by the lens system. Generally the drops off the centre of the image look smaller compared to the drops towards the side of the image.

The error of these three effects will be bigger at the side of the image. It is chosen to put a mask over the image. The aim is to limit the total surface of the image and so to exclude the area that is less precise. The choice for the diameter of the mask is discussed in section 4.6.

4.3.2 Subjective inaccuracy

Duplication error

An experiment is conducted to get an idea about the error when an experiment is duplicated. In this experiment a single drop is measured a hundred times after each other. This is done with two different drops. The results are depicted in Figure 4.8.

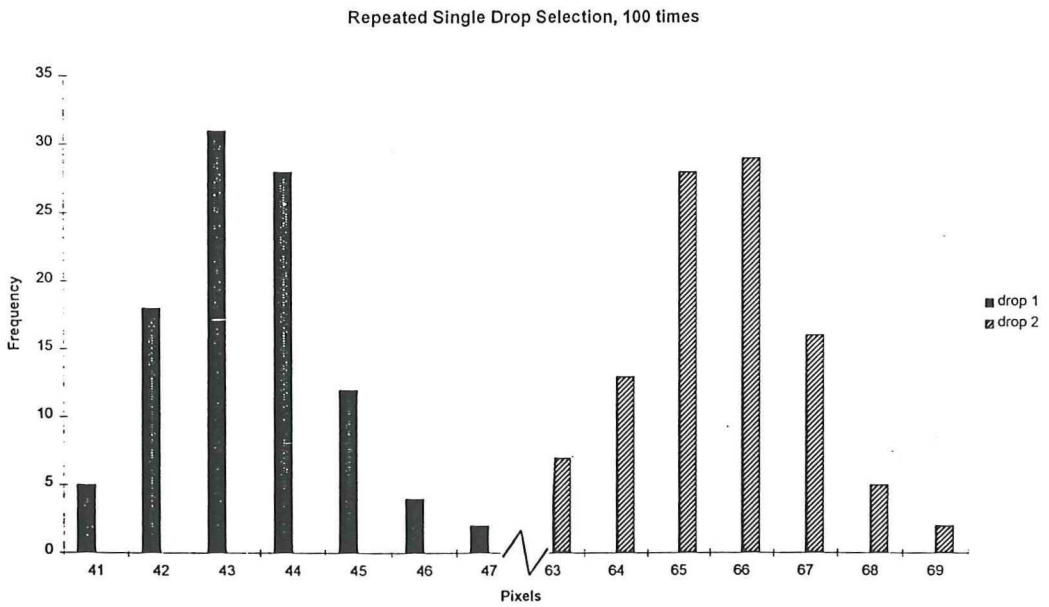

Figure 4.8 Repeating selecting 2 drops 100 times

The standard deviation in both cases was 1.3 pixels

difference between operators

The analysis of the images is done by a human operator. The analysis may differ. Shadows around drops ignored by one operator may be seen as drop boundaries by another operator. An experiment is conducted to see how serious this effect is. In the experiment two different persons measure drops of the same test distribution, using exactly the same set of pictures. To do so the operators only use the rules as stated in section (4.2). The two histograms of the distributions are given in fig(4.9).

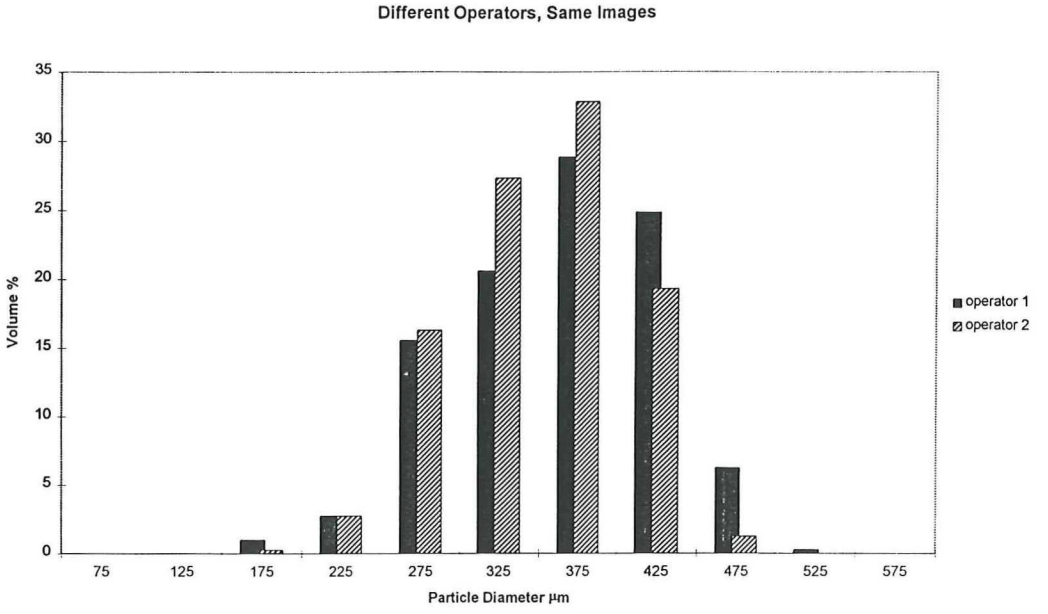

Figure 4.9 Two operators analysing the same pictures of a distribution. The total number of measured drops is 408 by both operators.

In this case Endoscope 1 is used with a calibration factor (see section 4.5) of 7.41 µm/pixel. The acquired parameters (see section 3) are depicted in Table (4.1). The differences for the d_{16}-d_{50} d_{50}-d_{84} parameters between the two operators are less then 2 pixels. The difference between the operators for the d_{16} parameter is 5.4 %. The average width, $(d_{16}-d_{84})/2$, showed a deviation of 25%.

	d_{84}	d_{50}	d_{16}	$d_{50}-d_{84}$	$d_{16}-d_{50}$	$(d_{16}-d_{84})/2$
operator 1	328	395	447	67	52	60
operator 2	328	380	425	52	45	48

Table 4.1 Different parameters (in µm) of a test distribution measured by two operators

Finite resolution of the eye.

The error resulting from placing the cursor is a simple consequence of the resolution of the human eye, the resolution and magnification of the screen, and the distance between the screen and the eye. In [20] it is concluded that the drop diameter can be measured with an accuracy of 2 to 4 pixels. Expressed in microns this means that the resolution is between 15 µm and 30 µm for endoscope1 and between 30 µm and 60 µm for endoscope2

The total error for the diameter ranges between 2 to 4 pixels.

4.4 Comparison with other methods

The endoscope drop size measurement video technique is compared with two other particle size methods. The first one is the Malvern particle sizer series(2600). The second drop size measurement method is the sieve method. As a test distribution solid EPS particles are used. The endoscope is put in the container of EPS particles without water as a continuous phase. In fig (4.10) and (4.11) are the results of the comparisons. In both cases 400 drops were counted by the EDSM. The drops counted by the EDSM are distributed in the same type of bins as the method where it is compared with.

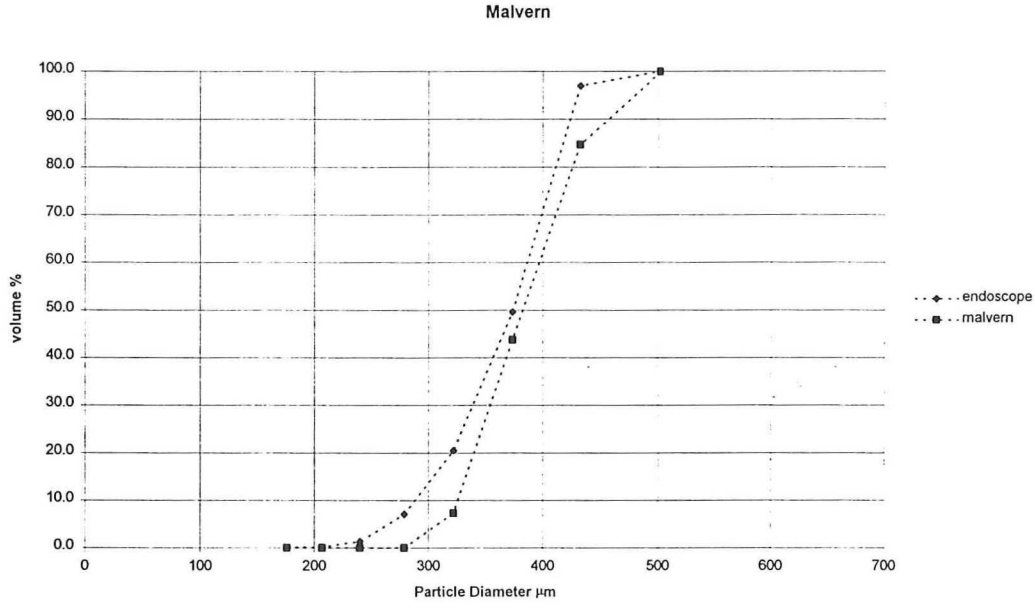

Figure 4.10 Cumulative volume distribution with Malvern and EDSM

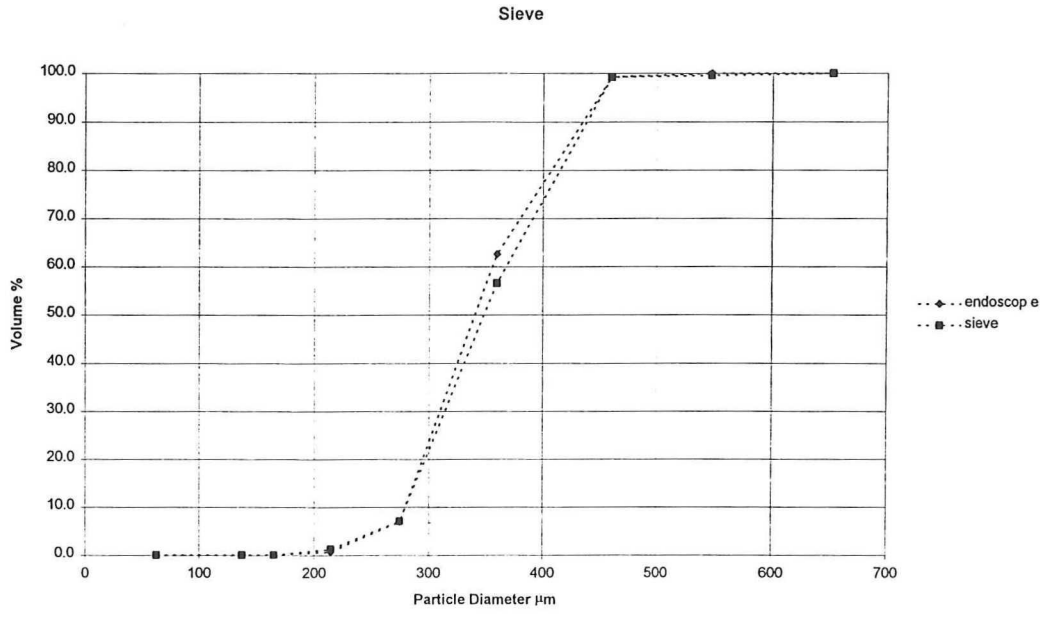

Figure 4.11 Cumulative volume distribution with sieve and EDSM

The accuracy of the Malvern is ± 4% on volume median diameter. The EDSM measurement lies within the Malvern error margin. The differences between the sieving and the EDSM are much smaller. It is generally assumed that sieving is a more accurate measurement method. But there are less bins then with the Malvern method.

In both cases the EDSM measured smaller particles than the other methods.

4.5 Calibration

To calibrate the system, the diameter of three different EPS particles are measured both with a measurement microscope and with the EDSM, see pictures 1 and 2.

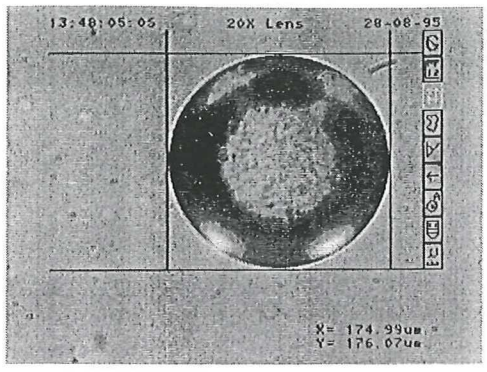

picture 1: The smallest EPS particle with the microscope

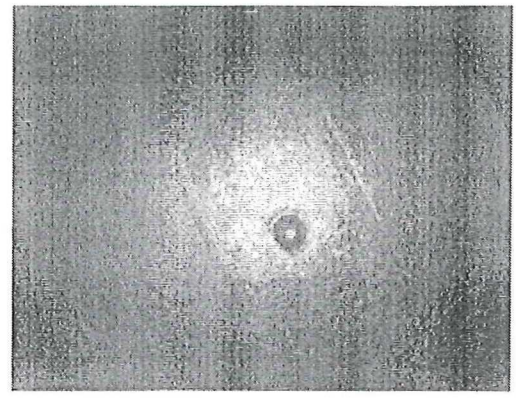

picture 2: The smallest EPS particle with the EDSM

The measurement microscope diameter is divided by the output of the image analysis program. The result is the calibration factor [μm/pixel].

$$C_f = \frac{D_{mm}}{D_{px}} \tag{4.1}$$

D_{mm} is the Diameter (in μm) of the measurement microscope, an Olympus BV 50 microscope with a Linkam VTO 323 videotext overlay. D_{px} is the diameter (in pixels) from the EDSM. The three calibration particles are fixed on the glass tube and moved over the total field of view. The data output file consists of the pixel radius and the co-ordinates. It was found for endoscope1 that by reducing the selectable area to half its diameter the deviation of the average pixel radius for three calibration particles reduced from 9.7 pixels to 3.5 pixels.(see table 4.2) This is shown in the graph (4.12). The relative deviation from the microscope value (in percentages) of the three calibration particles, is depicted versus their position (in pixels) from the centre of the image.

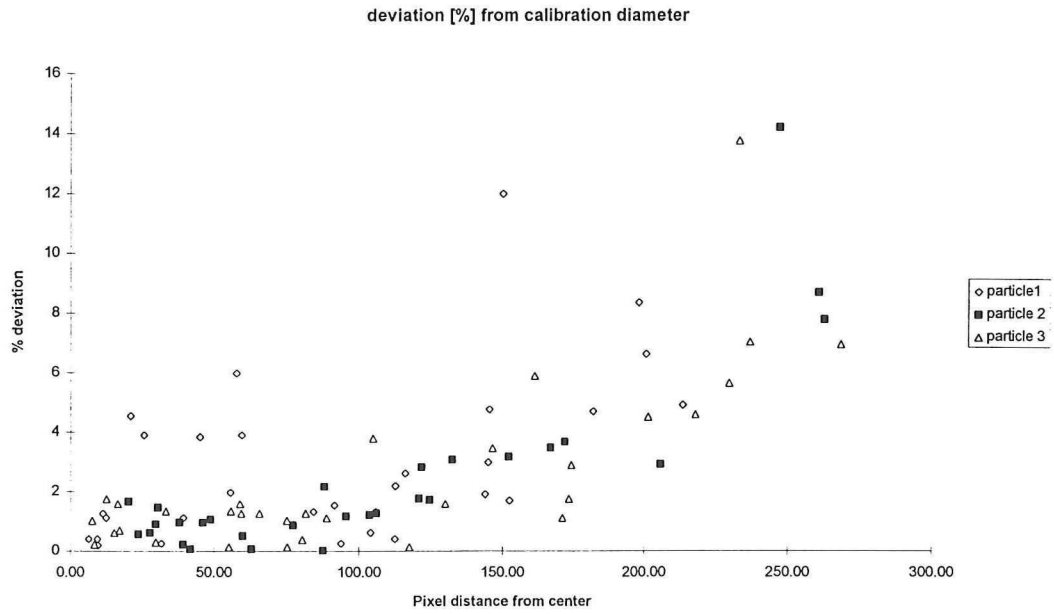

Figure 4.12 procentual deviation from the calibration diameter of three calibration particles.

area	particle1	particle2	particle3	average
no restriction	3.9	15.6	9.6	9.7
D_m=0.5 D	3.9	3.1	3.4	3.5

Table 4.2 Deviation (in pixels) of the calibration particle as a function of the image area

D_m [pixel] is the mask diameter and D_i [pixel] is the total diameter of the image As a result a mask is put over the image to decrease the total surface, and so to increase the accuracy. After the diameter of the image restricting mask was chosen, the average diameter is calculated. All the measured pixel diameters are multiplied with this calibration factor. The mask for endoscope1 had a diameter of 180 pixels and endoscope2 had a mask diameter of 130 pixels.

In the next table are the measured values of the calibration particles measured by the microscope and endoscope. Along with the calibration factor per calibration particle. Averaging the values will give the following calibration factors:

	microscope			endoscop1		endoscop2	
	D_{mm} x[μm]	D_{mm}y [μm]	D_{mm} [μm]	D_{px} [pixels]	factor	D_{px} [pixels]	factor
particle 1	175	176.1	175.6	24.2	7.26	8.8	20.03
particle 2	752	749	750.5	98.6	7.61	45	16.68
particle 3	447	449	448	60.7	7.41	27.8	16.14
C_f					**7.41**		**17.61**

Table 4.3 The measured diameters of the sample particles by the two endoscopes and microscope. And the calibration factor [μm/pixel].

The factor for endoscope 2 and particle 1 is higher then the other factors for endoscope 2. A reason for this might be the bigger relative error of 2 to 4 pixels for smaller particles. Another possible explanation is that the shadow around the particle (picture 2) makes it look bigger when selecting it. Chosen was to average anyway the three factors for the calibration factor C_f.

4.6 Conclusions and further improvements of the measurement method

4.6.1 Conclusions

The EDSM enables detailed observation of the structure of a dispersion revealing the presence of droplets-in-drops and distinguishing air bubbles from liquid drops. This method can distinguish drops ranging from 50 μm to 1.6 mm. In principle it is possible to measure everywhere in the vessel in any direction perpendicular to the endoscope. The only limitation is the length of the endoscope. Other advantages of this method are the relatively high frequency of data acquisition. This happens at a normal video frame rate of 50 frames a second.

Disadvantages are the intrusiveness of the system although the diameter of the endoscope is small, (8mm) compared to the tank (smallest tank diameter is 114 mm). Also the image processing is very time consuming. As shown in the example in section 4.2.5, Figure 4.6, it will take a great effort to determine the drops automatically.

4.6.2 Further work

Some improvements can still be made. First of all the method is time consuming. Directly grabbing images with the PC and processing them on the PC will save a considerable amount of time. The next step would be to automate the image processing programme. Advanced pattern recognition techniques are required for this. As well as a higher quality image with a better contrast.

Obviously the optical system is not precise enough and custom made endoscopes with less image deformation, might give a higher quality image.

A possibility to increase the contrast is the usage of colours. The light source has an in-build filter holder, so that the colour of the light can be altered easily. This feature in combination with a

coloured dispersed phase and a colour camera can give a better contrast. Discriminating drops in coloured images is less difficult to automate.

Although the illumination was sufficient for the conducted experiments it was not optimal. A high intensity stroboscopic light triggered by the camera could give better contrast and heat up the dispersion less. The EDSM is not yet tested deep inside dispersions. This requires a different illumination glass fibre holder.

5 Error estimation of measured drop-size distributions

In the previous chapter our drop size measurement method is explained. The errors when measuring individual drop sizes were discussed. In this chapter the inaccuracies in measuring drop-size distributions are treated.

5.1 Introduction

To obtain the drop size distribution in the ideal case all the drops in the vessel should be measured. In this research we are interested in the local drop size distribution so only a limited number of drops will be analysed. The number of drops to be analysed is important for the precision of the drop size distribution. To minimise the time required for the analysis of one population of drops, it is desirable to measure as few drops as possible. However the number must be sufficient to give an accurate result. In similar experiments in literature [19] it is concluded on empirical basis that a representative sample should not be smaller than 800 drops. This is the number above which a consistent mean size and distribution function resulted. Nothing was written about the imprecision when determining distributions from a smaller sample. To get an impression of the standard deviation of d_{16}, d_{50}, and d_{84}, as a function of the number of drops in a sample, a drop size measuring experiment was simulated. For this a Monte-Carlo technique was used.

5.2 Bias due to using a limited sized observation area

In section 4.5. the need to put a mask over the image that is to be analysed was described. Applying this mask increases the precision for measuring drop size distributions. An unwanted effect of this mask is that it introduces bias when measuring distributions. Two cases with for each case a different type of bias can be distinguished: The diameter of the mask is smaller than the diameter of the biggest drop in the distribution. Secondly, the mask diameter is bigger than the diameter of the biggest drop in the distribution. The effect of the first case is treated and simulated in section 5.4.4. The second case is explained in this section as well as simulated in section 5.4.4.

The total surface S_{max} of the image from the endoscope that can be covered by drops that will be validated with diameter r=0 is:

$$S_{max} = \pi \cdot R^2 \tag{5.1}$$

R is the mask radius, with $D_m=2 \cdot R$. Drops with diameter r are detected if their centres lay inside a circle, inside the mask. This circle has radius: $r_a=R-r$. This is illustrated in Figure 5.1.

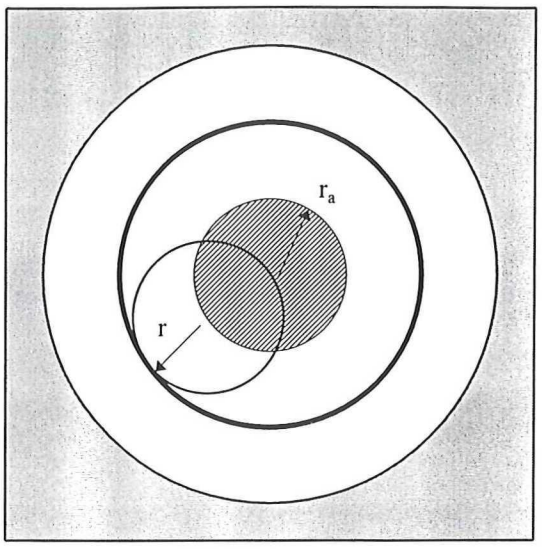

Figure 5.1 The selectable surface (hatched) for a drop with radius r.

Thus the total surface (hatched) of the image that can be covered by drop-centres equals:

$$S = \pi \cdot (R - r)^2 \tag{5.2}$$

r has values between 0 and R. (See Figure 5.1.) In terms of dimensionless numbers:

$$\hat{S} = \frac{S}{S_{max}} \tag{5.3}$$

and:

$$\hat{r} = \frac{r}{R} \tag{5.4}$$

Equation 5.2 becomes:

$$\hat{S} = (1 - \hat{r})^2 \tag{5.5}$$

The dimensionless surface equals the detection chance of a drop with radius $\hat{r}$ and its centre inside the mask. Equation 5.5 is plotted in Figure 5.2.

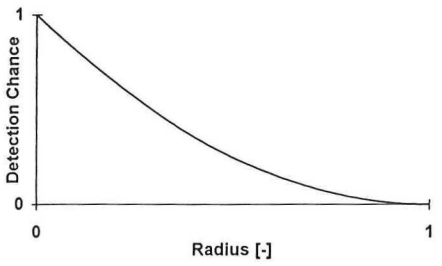

Figure 5.2 Detection chance of a drop with radius $\hat{r}$ and its centre inside the mask

It is obvious in Figure 5.2. that it is less likely for bigger drops to be detected.

5.3 Simulation programme

5.3.1 General description of the programme

The Turbo Pascal [25] program, (see Figure 5.3.) simulates measuring a fixed number of drops out of a number distribution, originating from a normal volume distribution. To simulate a selected drop a Monte-Carlo technique was used, see section 5.3.2. The randomly generated drop diameters are collected in bins of a certain width. The width corresponds with the calibration factor of the endoscope. In this way one bin equals one pixel. The acquired distribution is transformed into a volume distribution and the three parameter's d_{84}, d_{50}, d_{16} are calculated. This is repeated 1000 times. Then the average values for d_{84},d_{50}, d_{16} and their standard deviations σ_{84}, σ_{50}, σ_{16} are calculated. The programme then increases the number of drops in a sample and repeats this procedure. In this way the behaviour of the standard deviation, as a function of sample size can be studied. The calculated parameters are written to a file with extension .mcm. This file can be easily imported to a Microsoft Excel worksheet. The programme simulates either with or without a mask. In the first case the grey branch in the flowchart is followed (see Figure 5.3) after the 'hit?'-box. In the latter case the grey branch may be ignored. How the mask is simulated, is explained in section 5.3.2.

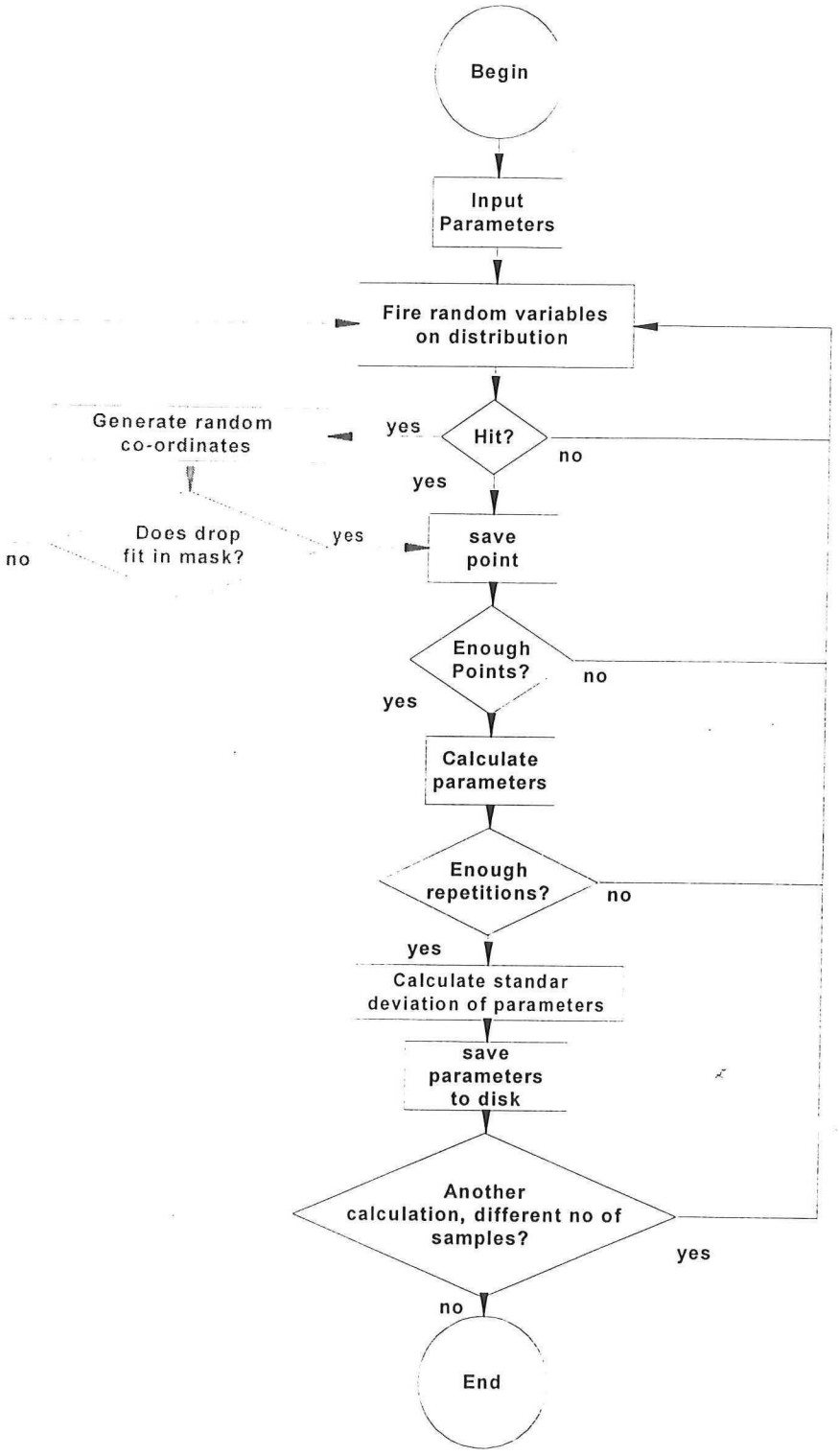

Figure 5.3 Flowchart of the programme. The grey branch is followed for the simulation with the mask.

5.3.2 Monte Carlo method

A Monte-Carlo technique is used [12] to generate non-uniform random variables. It is called the rejection method for continuous random variables. If the probability density function f(x) is non-zero over only a finite range then it is easy to box it in, as shown in fig 5.4. Using U(0,1) random variables it is a simple matter to sprinkle points uniformly and randomly over the rectangle shown, simply by taking points with Cartesian co-ordinates $(\theta+(\alpha-\theta)U_1,\delta U_2)$. Where U_1 and U_2 are independent U(0,1) random variables (a random value between 0 and 1). Points above f(x) are rejected, while points below f(x) are accepted. We take $\theta+(\alpha-\theta)U_1$ as a realisation of X.

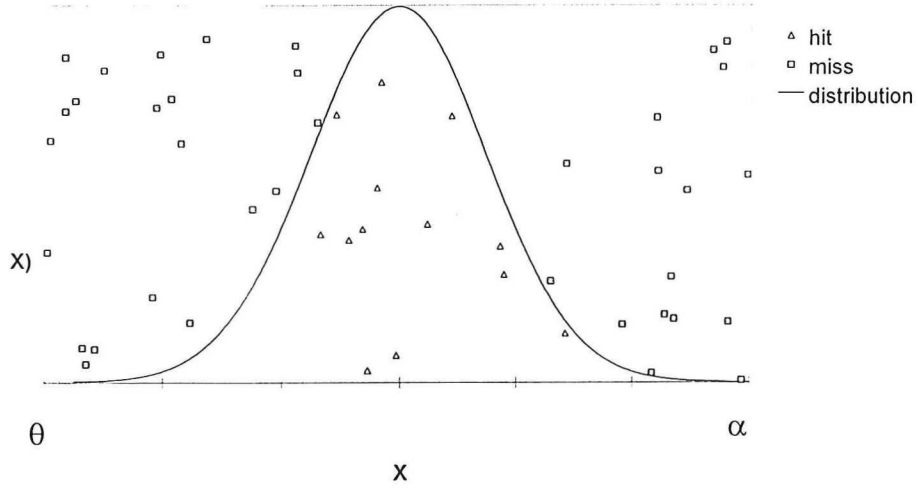

Figure 5.4. Sampling from the probability density function f(x) with the rejection Monte Carlo Method

There is a snag with the above approach: the probability of rejection could become quite large if the density f(x) has a spiked form like in Figure 5.5.(C), and the surface under the graph becomes small. To box the number distribution in, the maximum of the function has to be known. There are two possible maxima: If the σ_d of the distribution is large compared to the μ_d the maximum of the distribution is at the smallest detectable drop diameter d_{min}. The latter is set to 5 pixels for endoscope-2. See Figure 5.5(C). Otherwise it is at:

$$\frac{d(f_n(d))}{d(d)} = 0 \tag{5.6}$$

Where $f_n(d)$ is equation (2.5). The solution for this equation is:

$$d = \frac{\mu_d + \sqrt{\mu_d{}^2 - 12\sigma_d{}^2}}{2} \qquad \text{if} \qquad \mu_d \geq \sqrt{12}\,\sigma_d \tag{5.7}$$

See fig 5.5. A and B. The values at both local maxima have to be compared to select the highest one.

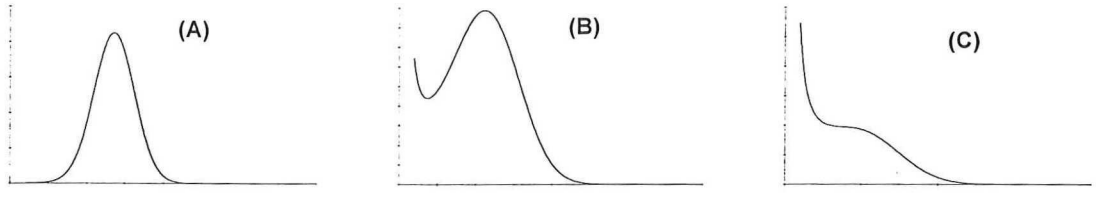

Figure 5.5. Three different number distributions from a normal volume distribution with μ_d is 600 μm for A, B and C. And σ_d is 100 μm (A), 150 μm (B) and 175 μm (C)

In the simulation of the mask, another two extra random variables are generated. They simulate the co-ordinates where a drop may be situated. The random co-ordinates are transformed to pixel co-ordinates with:

$$x = U(0,1) \cdot D_m - \frac{D_m}{2} \qquad \text{and} \qquad y = U(0,1) \cdot D_m - \frac{D_m}{2} \tag{5.8}$$

With x and y as the random pixel co-ordinates and U(0,1) as a random variable. In this way two random co-ordinates are created in a box, exactly containing the mask. The program accepts a drop if equation 5.9. is true.

$$\sqrt{x^2 + y^2} + d \leq \frac{D_m}{2} \tag{5.9}$$

5.4 Results

The input parameters are chosen to simulate the distributions measured with Endoscope2. The width of the bins corresponds to the Calibration factor (C_f=17.61 μm). This is because the EDSM output is in pixels. The endoscope has a finite resolution. For the simulations it was chosen to take 5 pixels as a minimum diameter for a droplet. The smallest detectable drop diameter d_{min} then equals 4.5·17.61=79 μm

5.4.1 Without the use of a mask

A number of simulations was done to examine the behaviour of σ_{84}, σ_{50}, σ_{16} as a function of the number of drops in a sample. This for distributions typical for the endoscope experiments with σ_d ranging from 100 to 175 μm and μ_d ranging from 500 to 700 μm. The maximum allowed drop diameter is in all cases chosen to be 1600 μm. The values for σ_{84}, σ_{50}, σ_{16} decrease with the number

of drops in a sample, in accordance with eq. 5.10. This is shown in the figure (5.6). Sampled is from a μ_d=600 μm, σ_d =150 μm distribution.

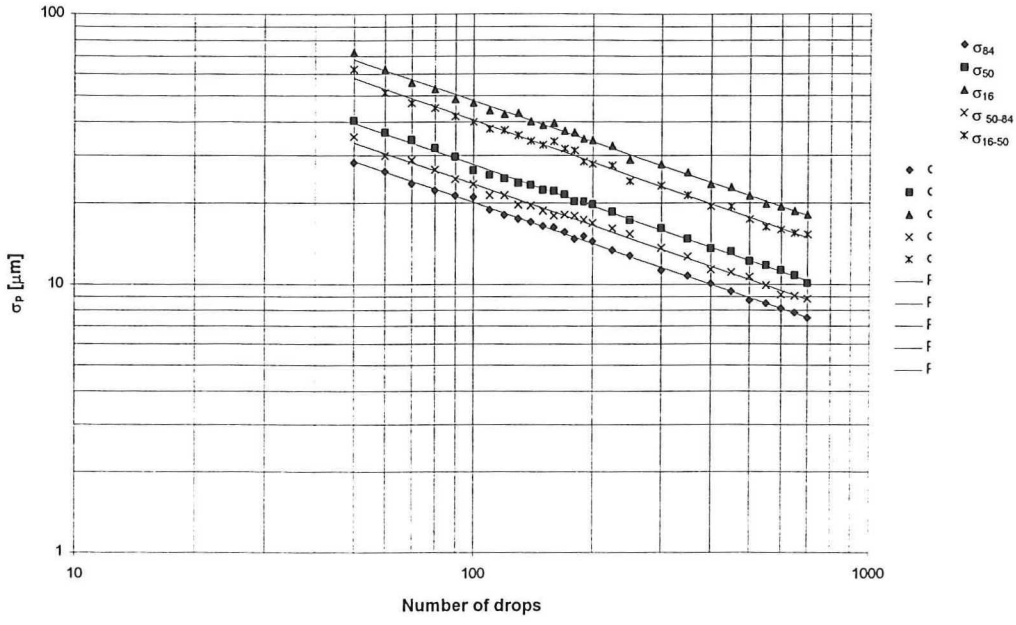

Figure 5.6 Parameter-standard deviation of 1000 realisations of a μ_d=600 μm, σ_d =150μm distribution vs. Number of drops in a sample.

The general form of σ_{84}, σ_{50}, σ_{16} is:

$$\sigma_p = \frac{C}{\sqrt{N}} \tag{5.10}$$

Where C is a constant depending on the distribution parameters: μ_d and σ_d. In the next table the values for C are given. The values are calculated from the output of the simulation with the Least Square Method. Out of (5.10) the number of samples can be calculated given a fixed allowable standard deviation σ_p. This is done in table 5.2 for a standard deviation of 17.61 μm which is the equivalent of 1 pixel.

μ_d		σ_d 100	125	150	175
500	d_{84}	120	164	224	293
	d_{50}	152	224	334	481
	d_{16}	247	390	609	921
	d_{50}-d_{84}	137	191	267	366
	d_{16}-d_{50}	212	325	497	751
600	d_{84}	123	152	199	262
	d_{50}	143	195	275	391
	d_{16}	218	322	474	701
	d_{50}-d_{84}	131	174	234	318
	d_{16}-d_{50}	189	274	393	580
700	d_{84}	122	151	189	233
	d_{50}	135	181	238	322
	d_{16}	203	287	393	551
	d_{50}-d_{84}	131	169	213	277
	d_{16}-d_{50}	180	248	340	471

Table 5.1. Results of simulations, constants for calculating σ_p.

μ_d		σ_d 100	125	150	175
500	d_{84}	47	87	162	276
	d_{50}	74	162	359	746
	d_{16}	197	491	1197	2737
	d_{50}-d_{84}	61	117	229	433
	d_{16}-d_{50}	145	342	797	1821
600	d_{84}	48	75	127	222
	d_{50}	66	123	243	493
	d_{16}	153	335	724	1587
	d_{50}-d_{84}	55	98	177	325
	d_{16}-d_{50}	115	241	499	1085
700	d_{84}	48	73	115	175
	d_{50}	59	106	183	334
	d_{16}	134	266	497	980
	d_{50}-d_{84}	55	92	146	248
	d_{16}-d_{50}	104	199	373	715

Table 5.2. The number of drops in a sample required for measuring d_p with a standard deviation of 1 pixel or 17.61 μm.

5.4.2 Deviation after duplication

To see what the variation is in the simulation values, a simulation is done 40 times with the same number of drops in a sample, and 1000 repetitions. The simulation is on basis of a μ_d=600 μm, σ_d =150 μm distribution. In table (5.3) are depicted the average values and their procental deviation.

	d_{84}	d_{50}	d_{16}	d_{50}-d_{84}	d_{16}-d_{50}
average	451.11	600.19	749.54	149.08	149.35
deviation %	0.12	0.18	0.25	0.46	0.87

	σ_{84}	σ_{50}	σ_{16}	σ_{50}-σ_{84}	σ_{16}-σ_{50}
average	8.89	12.27	21.12	10.39	17.75
deviation %	5.46	4.78	4.42	5.08	4.80

Table 5.3. Deviation of d_p and σ_p after duplication of the experiment.

In this distribution theoretically d_{50} should be 600 mm, d_{84} should be μ_d -σ_d μm and d_{16} should be μ_d +σ_d μm (450 μm and 750 μm). There is slight difference between the results and input values. This is due to the discretisation of the distribution and linear interpolation afterwards to obtain d_p. The deviation of d_p is in all cases small. The deviation of σ_p is larger than the deviation of d_p, about 5 % of the average value.

5.4.3 Minimal detectable drop size.

As the endoscope has a finite resolution, only drops that are big enough could be distinguished and measured. This effect is simulated with a μ_d=600 μm, σ_d =150 μm distribution. The minimum detectable diameter is varied between 100 to 400 μm. The theoretical values are found by solving the equation (5.11).

$$\frac{\int_{d_p}^{\infty} \frac{e^{\left(-\frac{(d-\mu_d)^2}{2\sigma_d^2}\right)}}{\sigma_d\sqrt{2\pi}}\,d(d)}{\int_{d_{min}}^{\infty} \frac{e^{\left(-\frac{(d-\mu_d)^2}{2\sigma_d^2}\right)}}{\sigma_d\sqrt{2\pi}}\,d(d)} = \frac{p}{100} \qquad \text{for } p = \{16, 50, 84\} \qquad (5.11)$$

Where d_{min} is the minimal detectable drop size. The values for d_p are calculated numerically and depicted in figure (5.7). along with the results of the simulation

The measured distribution widths are affected significantly if the minimal detectable drop has a diameter bigger than 365 μm. Then the d_{50}-d_{84} parameter has a deviation of 17.61 μm which equals 1

pixel with endoscope-2. See figure (5.7).The parameter d_{50}-d_{84} is chosen as it is the most critical variable in this case.

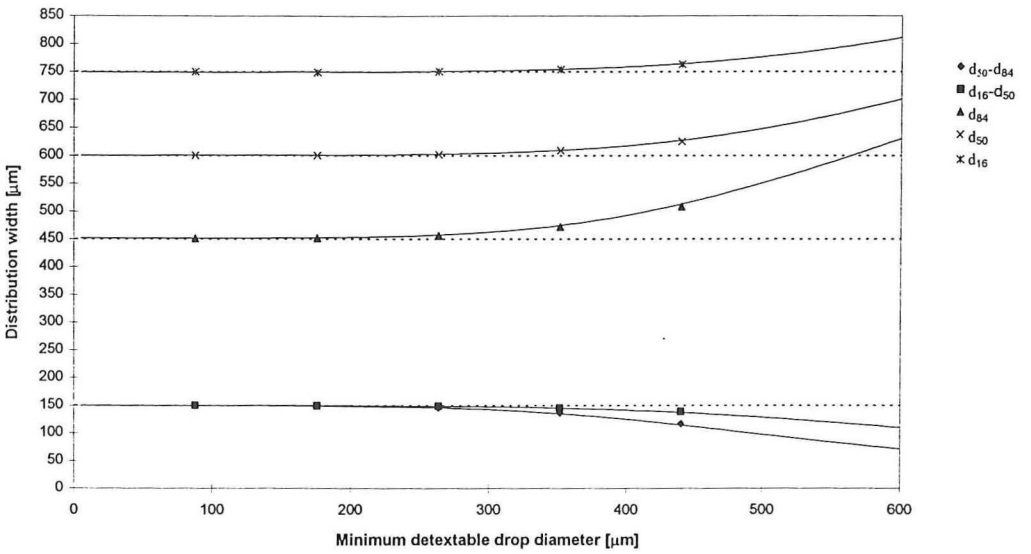

Figure 5.7 Distribution width [µm] vs. the minimum detectable drop diameter d_{min} [µm] in a μ_d=600 µm, σ_d=150 µm distribution. Both simulated in the programme and calculated numerically

5.4.4 Influence of a mask

The usage of a mask causes, as explained in section (5.2), bias. The d_{84}, d_{50}, d_{16} values tend to decrease with decreasing mask diameter D_m. This is simulated for a μ_d=600 µm, σ_d=150 µm distribution. The simulations are based on 1000 repetitions and a sample of 1000 drops.

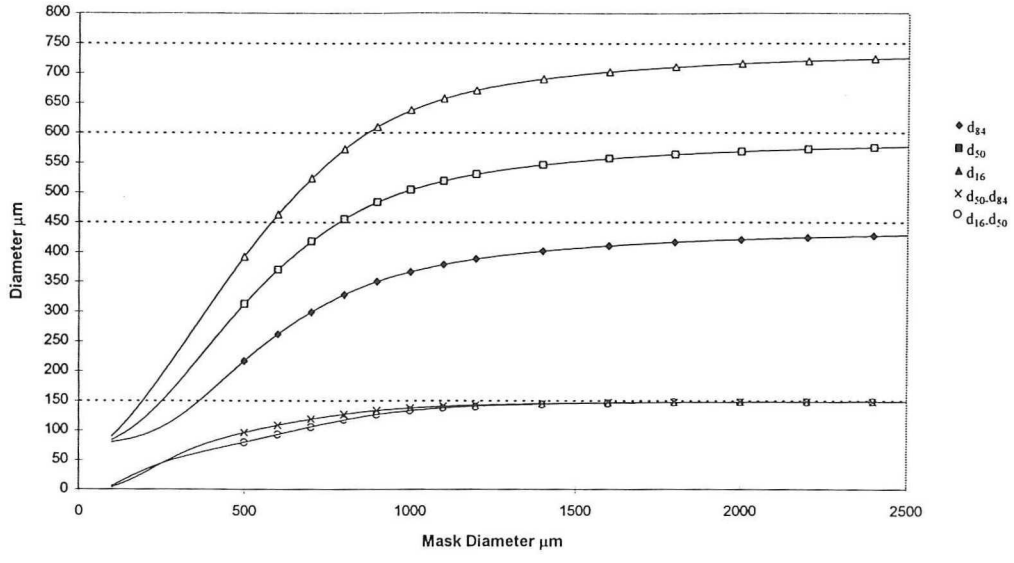

Figure 5.8. Diameter parameters vs. mask diameter in a μ_d=600 µm, σ_d=150 µm distribution. Both from the simulation programme and calculated numerically.

The d_p can be found analytically by solving formula (5.12). The d_p parameter is a function of D_m, σ_d, and μ_d. The result is depicted in Figure 5.8 along with the values of the Monte Carlo simulation

$$\frac{\int_{d_p}^{\infty} \frac{e^{\left(-\frac{(d-\mu_d)^2}{2\sigma_d^2}\right)}}{\sigma_d\sqrt{2\pi}} \cdot (1-\frac{d}{D_m})^2 \, d(d)}{\int_{0}^{\infty} \frac{e^{\left(-\frac{(d-\mu_d)^2}{2\sigma_d^2}\right)}}{\sigma_d\sqrt{2\pi}} \cdot (1-\frac{d}{D_m})^2 \, d(d)} = \frac{p}{100} \qquad \text{for } p = \{16, 50, 84\} \qquad (5.12)$$

The formula can be interpreted in the following way: It is the multiplication of the number drop-size density with the detection chance (fig 5.2 equation 5.5) from which d_p is calculated.

This is illustrated in figure(5.9) for a volume distribution $f_v(d)$ with μ_d=600µm and σ_d=150µm. The minimum detectable drop size d_{min} is 79 µm. The volume distribution (see Figure A) is transformed to a number distribution $f_n(d)$ (see Figure B). This distribution is multiplied with equation 5.5. In this example for D_m = 700 µm (see Figure C). The result is the biased number distribution (see Figure D). This number distribution is transformed back to its volume distribution (see Fig E).In Fig F are shown the unbiased (right) and the biased (left) cumulative volume distributions. The characteristic distribution parameters, d_p shift towards the left when a mask is applied. In the experiments the mask

had a diameter of 130 pixels or 2.35 mm. The influence of the mask is neglectable in the experimental set-up.

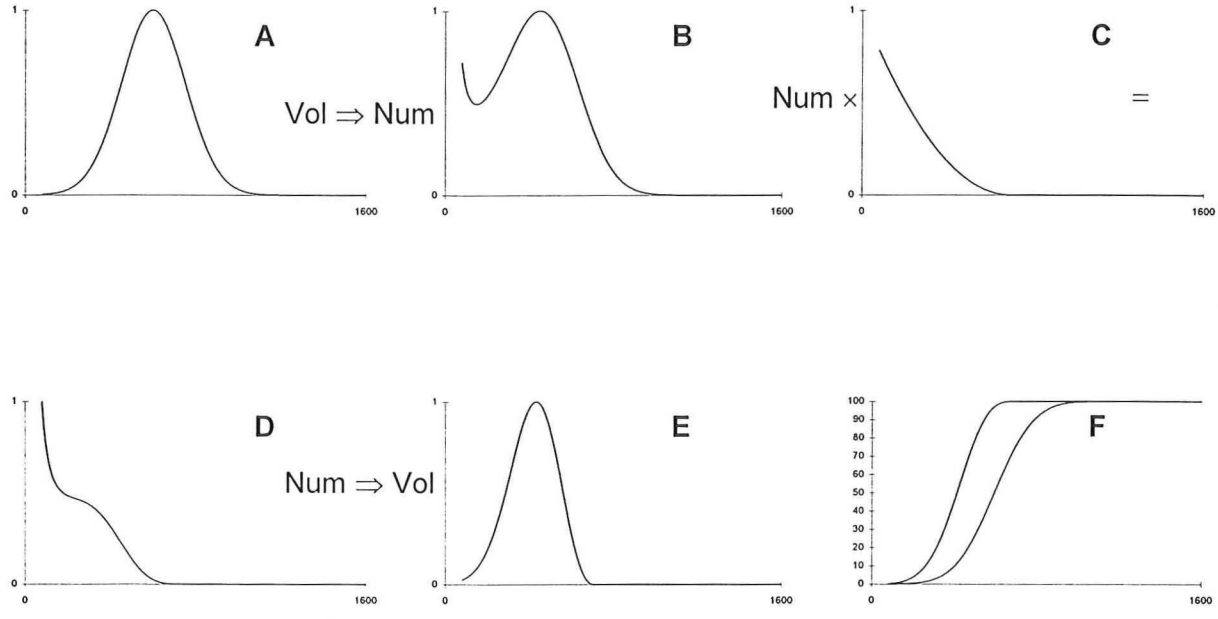

Figure 5.9. Graphical representation for calculating d_p. (μ_d=600μm, σ_d=150μm, D_m= 700). The minimum detectable drop size is 79 μm.(A) unbiased volume distribution. (B) number distribution. (C) Bias function. (equation 5.5) (D) Biased number distribution. (E) Biased volume distribution. (F). Biased (l) and unbiased (r) volume cumulative distribution.

The measured distribution widths are affected significantly in the case of the simulated distribution, if the mask has a diameter smaller than 1000 μm. The d_{16}-d_{50} has a deviation of 17.61 μm which equals 1 pixel with endoscope-2. See Figure (5.8). The d_{16}-d_{50} parameter is chosen as it is the most critical one in this case.

The standard deviation σ_{84}, σ_{50}, σ_{16} of the d_{84}, d_{50}, d_{16} also decreases with decreasing D_m. This is depicted for the same distribution and simulation in figure(5.10). The standard deviation σ_p follows the trend of the diameter parameters d_p.

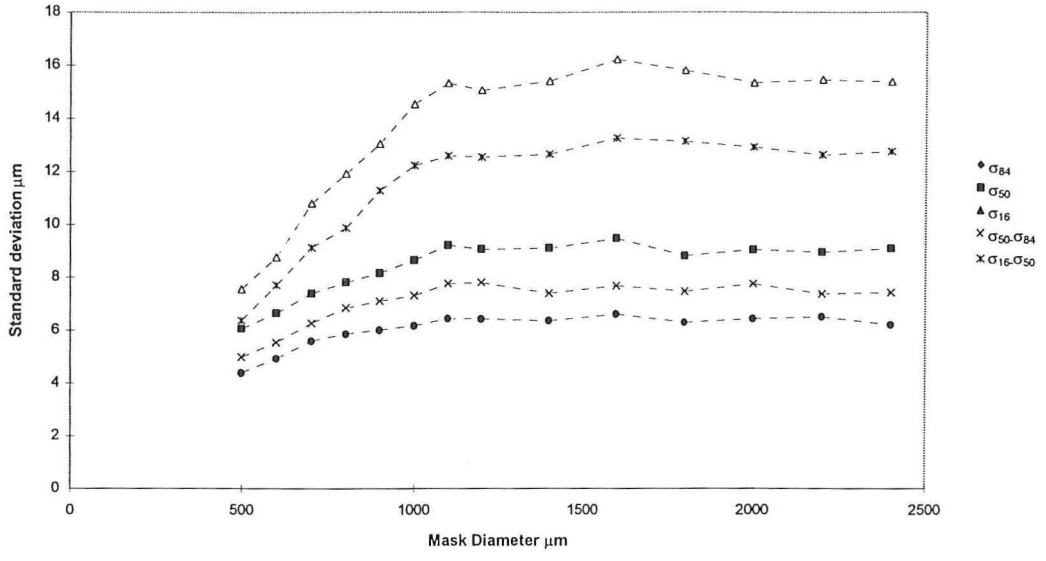

Figure 5.10 Standard deviation parameters vs mask diameter in a μ_d=600 µm, σ_d=150 µm distribution

5.5 Conclusions

The simulations show that the value of the standard deviation σ_p of the parameter's that describe the distribution, d_p, decrease when more drops are measured.

The simulation also showed that the value of the standard deviation σ_p of the parameter's that describe the distribution, d_p, increases when the standard deviation of the distribution increases.

The value of the standard deviation σ_p of the parameter's that describe the distribution, d_p, decreases when the mean of the distribution increases.

The minimal detectable drop size is not very critical. In the μ_d=600µm, σ_d=150 µm case, no significant effect on the distribution-width was seen if the minimal detectable drop was as big as 365 µm. In the experiments, it was 79 µm.

Applying a mask has an effect on the values of the typical parameters of a drop size distribution. The effect is bigger for d_{84}, d_{50}, d_{16} than for d_{50}- d_{84} and d_{16}- d_{50}. In the μ_d=600 µm, σ_d=150 µm case no significant deviation in d_{50}-d_{84} and d_{16}-d_{50} showed if the mask diameter D_m was bigger then roughly 1000 µm. This value is about two times the mean of the distribution.

6 Results and discussion

Before starting the discussion of the final results, first an overview of relevant theory will be given about shapes of distributions. Then the experimental results will be presented. First the effect power input on drop size distribution at the three different scales are presented. Then the same results are presented in a different manner: the effect of scale at constant power input. At the end the results will be compared with literature.

6.1 Signal analysis

6.1.1 Transformation from raw data to drop size distribution

As stated in section 4.2.5 the output of the image analysis program is a file containing the drop diameter (in pixels) and location. A typical histogram of the image drop diameters in (μm) of this output file is shown in figure (6.1). A measurement consists of 500 drops.

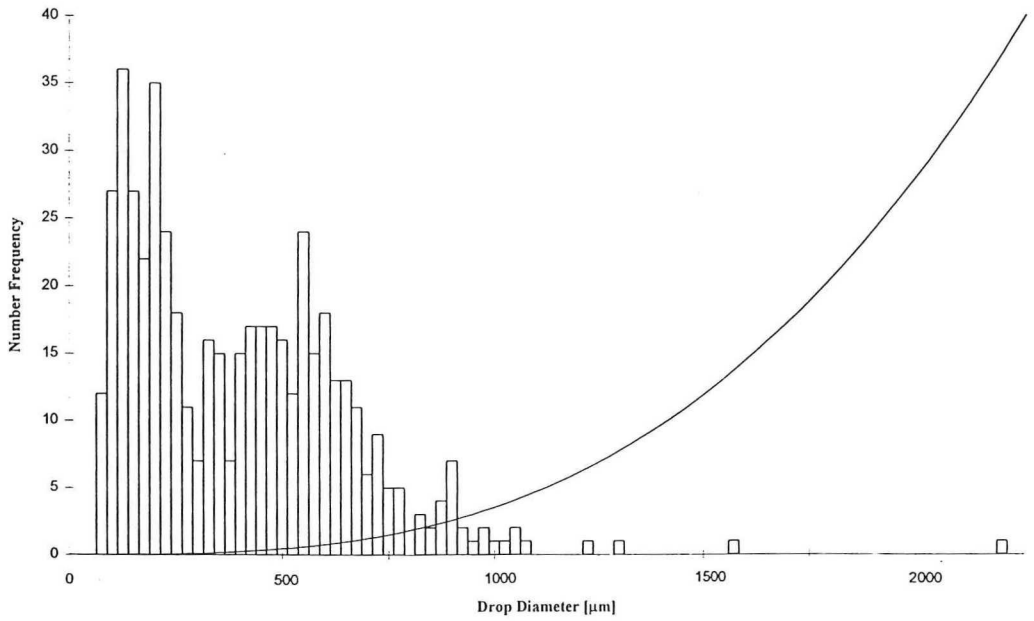

Figure 6.1 Number distribution histogram of the drop size measurement experiment in the medium vessel with medium power input. The line represents the relative volume per diameter.

The transformation of a number to a volume distribution is calculated with equation (3.12) and multiplied with 500 to obtain the same surface in the chart for better comparison. This formula can be interpreted as multiplying the number distribution with the line drawn in the figure above ($\sim d^3$). The volume distribution is shown in Figure (6.2).

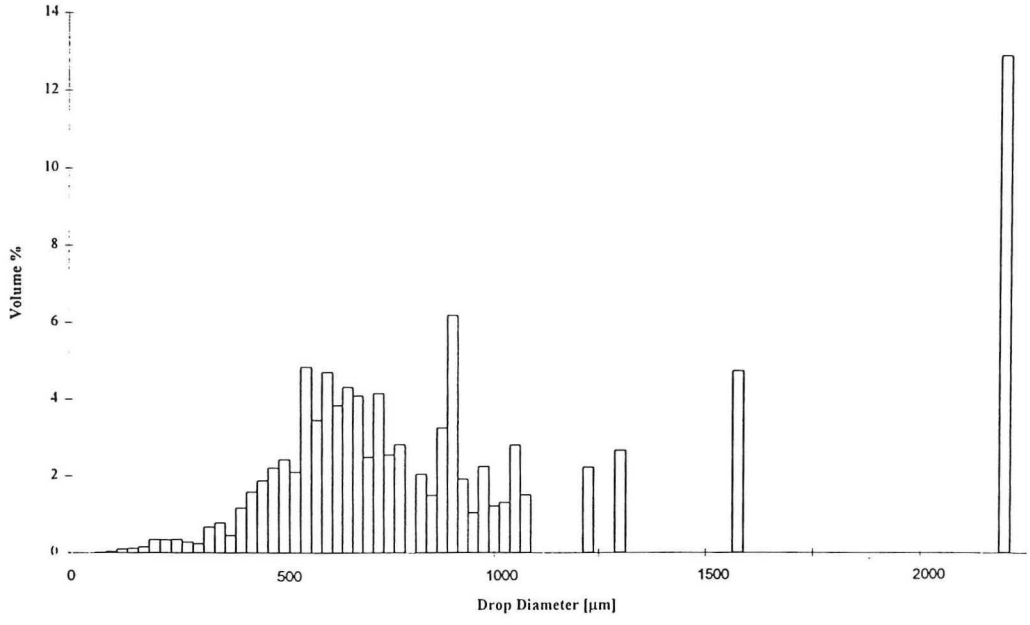

Figure 6.2 Volume distribution histogram of the drop size measurement experiment in the medium vessel with medium power input. Notice the one drop on the right hand side representing 12.9 % of the total volume.

The volume distribution reveals that a limited number of big drops represent a large fraction of the total volume. For this example, the biggest drop (with d = 1550 µm) represents 12.9 % of the total volume. The effect of this single drop on the cumulative drop size distribution is shown in the next Figure, Fig (6.3). Here the cumulative volume distribution is showed of the above experiment with and without the biggest drop taken into account.

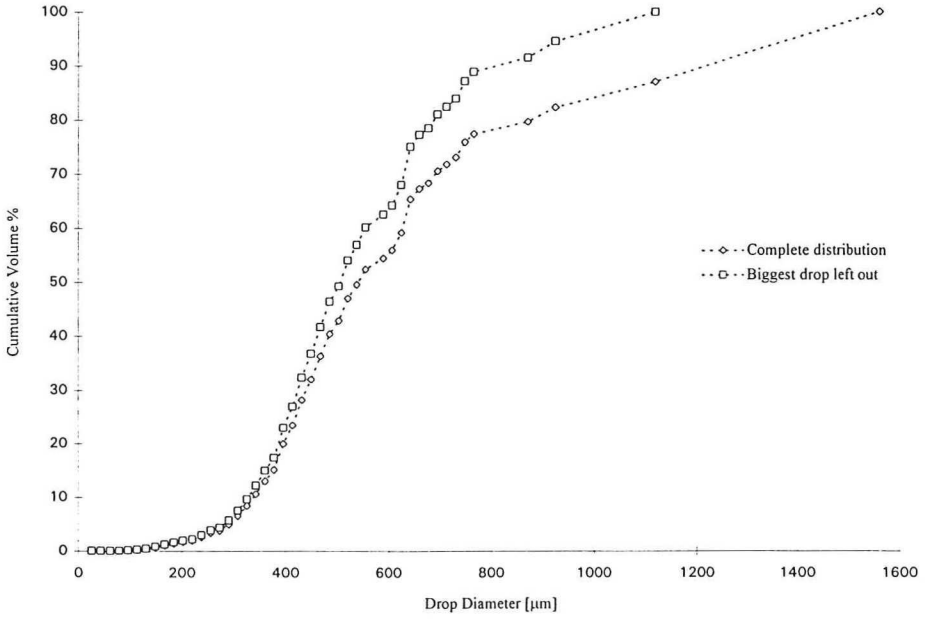

Figure 6.3 Cumulative Volume Distribution of the drop size measurement experiment in the medium vessel with medium power input. Both curves are from the same experiment and show the influence of the biggest drop on the total volume. The biggest drop is left out in the left curve.

6.2.3 The determination of the shape of a drop size distribution

In this section different shapes of distributions are compared with a typical distribution from the experiments. The aim of this section is to give a qualitative impression on determining shapes, not to give quantitative values of parameters describing the distribution. As an example we take the distribution of the experiment in the medium vessel with the high power input. This distribution is compared with a single normal distribution and a bimodal distribution.

- Normal distribution:

As explained in section 2.4, a normal distribution, see Fig(6,4) has a cumulative distribution shaped like in Fig (6.5).

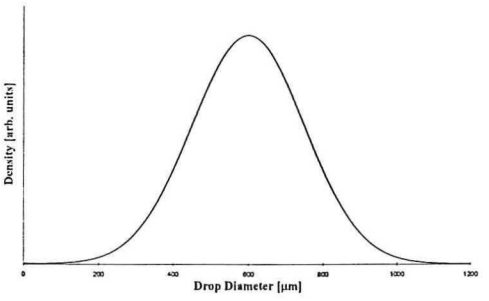

Figure 6.4 Example of a normal volume distribution.

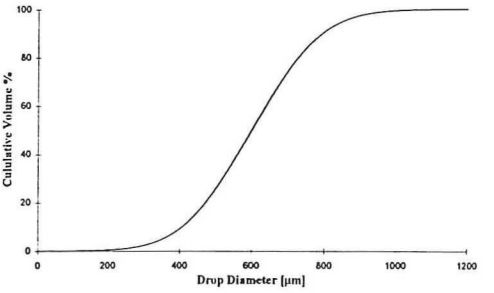

Figure 6.5 Example of a cumulative distribution from a normal distribution.

The distributions in the above graphs are calculated with equation (6.1) with μ_d is 600 µm and σ_d is 150 µm.

The experimental values of this typical case are fitted according to the least squares method with a cumulative normal distribution. The result is shown in Figure (6.6).

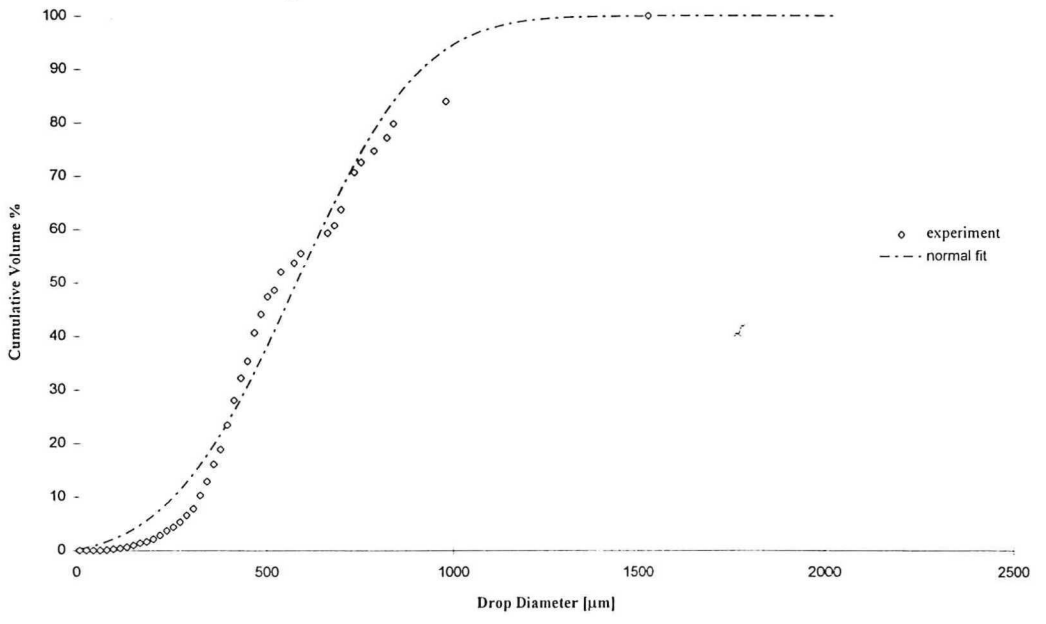

Figure 6.6 Cumulative volume distribution of the drop size measurement experiment in the medium vessel with high power input fitted with a normal distribution.

In this case the values for the parameters of the fitting equation are given by μ_d is 574 µm and σ_d is 262 µm. The fitted normal distribution seems not to correspond very well with the experimental data.

- Bimodal distribution:

A bimodal distribution is the sum of two normal distributions. The equation for this is:

$$f_{v,b}(d) = c_1 \left(c_2 \frac{e^{\left(-\frac{(d-\mu_{d1})^2}{2\sigma_{d1}^2} \right)}}{\sigma_{d1}\sqrt{2\pi}} + (1-c_2) \frac{e^{\left(-\frac{(d-\mu_{d2})^2}{2\sigma_{d2}^2} \right)}}{\sigma_{2d}\sqrt{2\pi}} \right) \tag{6.1}$$

Where c_1 is a scaling constant and c_2 a weighting factor for both normal distributions. The next two figures give a graphical representation of a bimodal distribution: On the left the volume density function and right the cumulative volume distribution.

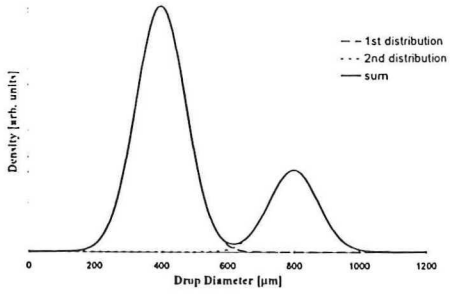

Figure 6.7 Example of a bimodal volume distribution

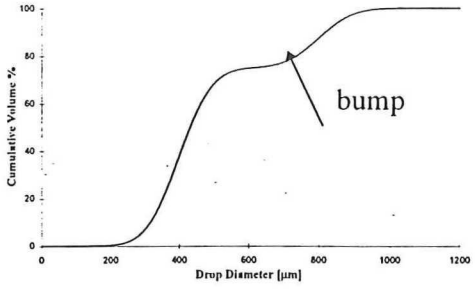

Figure 6.8 Example of the cumulative bimodal volume corresponding with fig 6.7

The values of the parameters of equation (6.1) used for the example are for μ_{d1} and μ_{d2} 400 and 800 µm. The values for σ_{d1} and σ_{d2} are both 75 µm. The value used for c_2 is 0.75. The constant c_1 is scaled in such a way that the total surface of the bimodal volume distribution is 1, or:

$$\int_0^\infty f_{v,b}(d)\,d = 1 \tag{6.2}$$

The bimadality of the distribution is translated into a bump in the cumulative volume distribution. In the next Figure the experimental volume drop size is fitted to a bimodal distribution according to equation (6.1). The least square method is used for this.

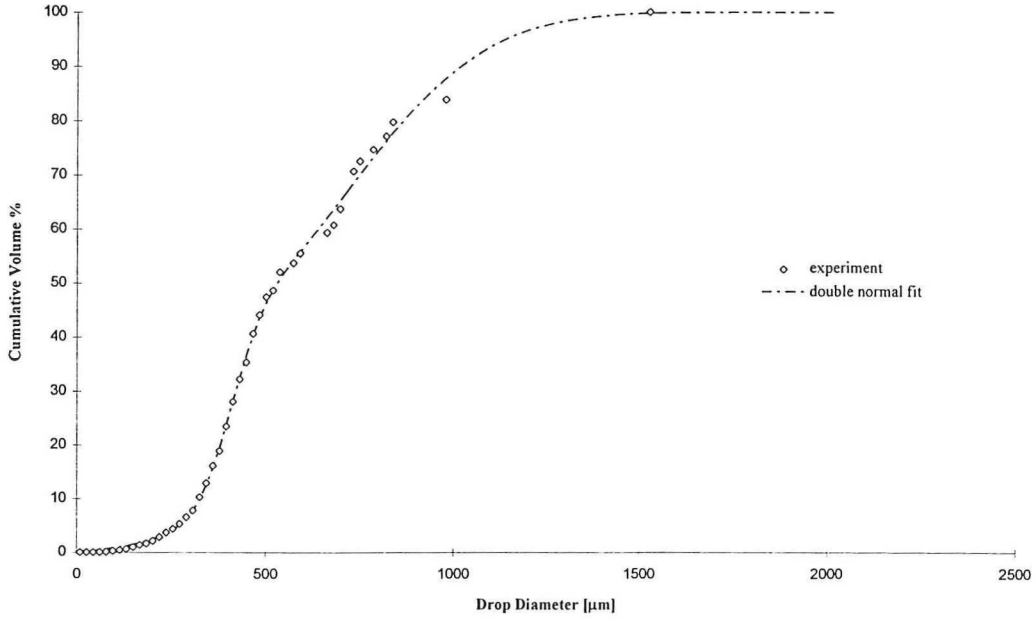

Figure 6.9 Cumulative volume distribution of the drop size measurement experiment in the medium vessel with high power input fitted with a bimodal distribution.

The values of the parameters of equation (6.1) used to fit the experimental volume drop size distribution are for μ_{d1} and μ_{d2} 407 and 706 µm respectively. The values for σ_{d1} and σ_{d2} are 67 and 294 µm. The value used for c_2 is 0.32. The bimodal distribution fits the experimental distribution better than the simple normal distribution. This is not surprising as the formula for a bimodal distribution has more fit parameters. The drop size volume distribution histogram and the fitted bimodal function are depicted in the next figure:

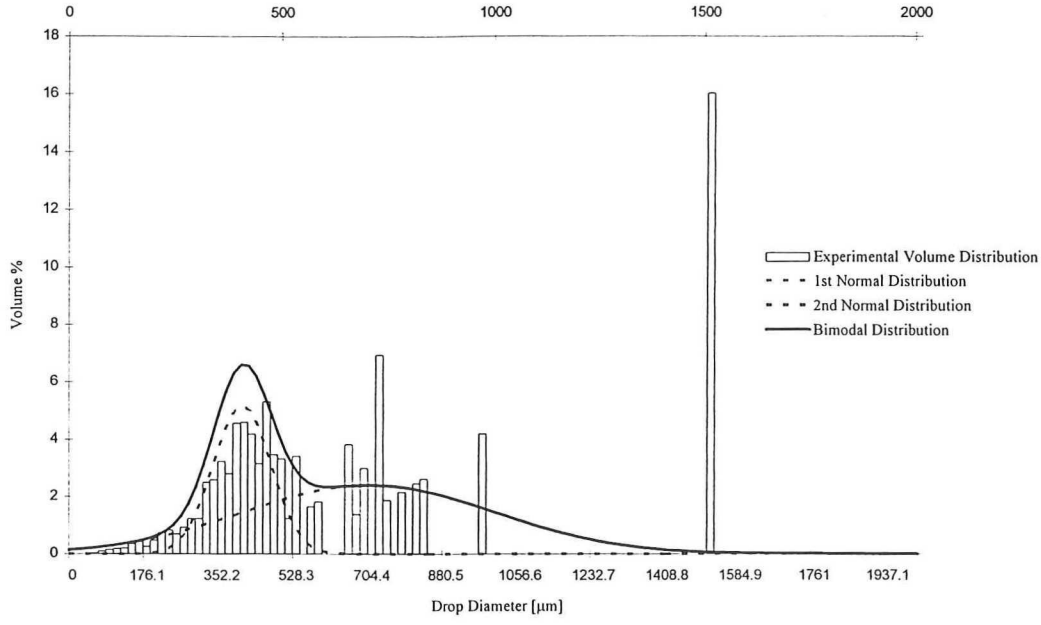

Figure 6.10 Volume distribution of the drop size measurement experiment in the medium vessel with high power input fitted with a bimodal distribution.

6.2 The effect of power input at individual scales

Hereafter are shown the measured cumulative volume distributions for respectively the large, medium and small vessel. The 3 different measurements are for the three different power-inputs: 0.20, 0.25, and 0.31 W/kg. Error margins are calculated for the calculated parameters (d_{16}, d_{50} and d_{84}) and given in section 6.3 (table (6.1))

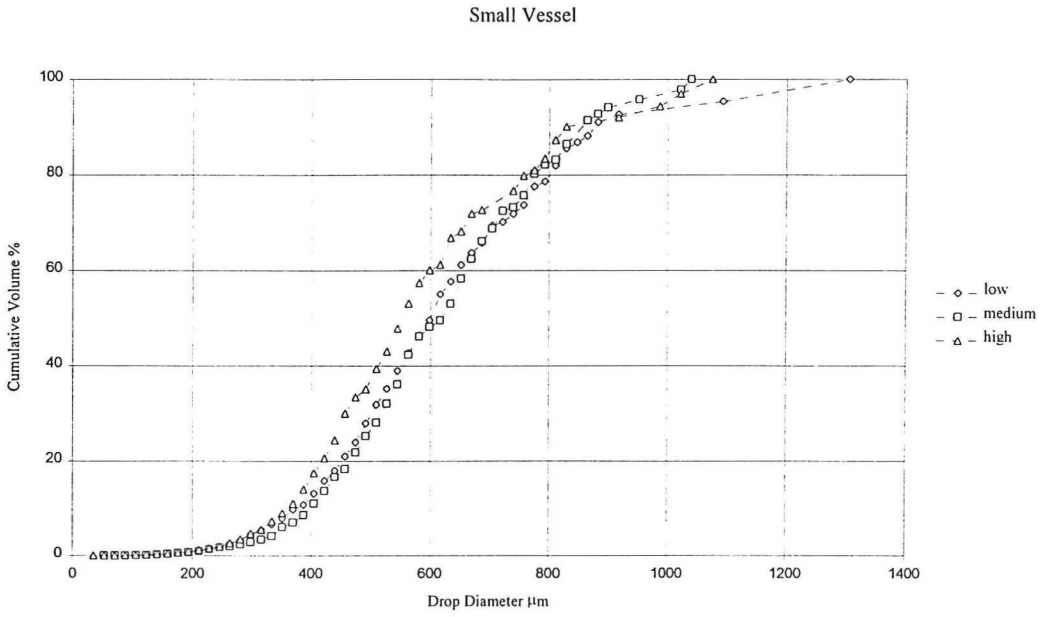

Figure 6.11 Cumulative volume distribution for three different power inputs in the small vessel. Each sample consists of 500 drops measured.

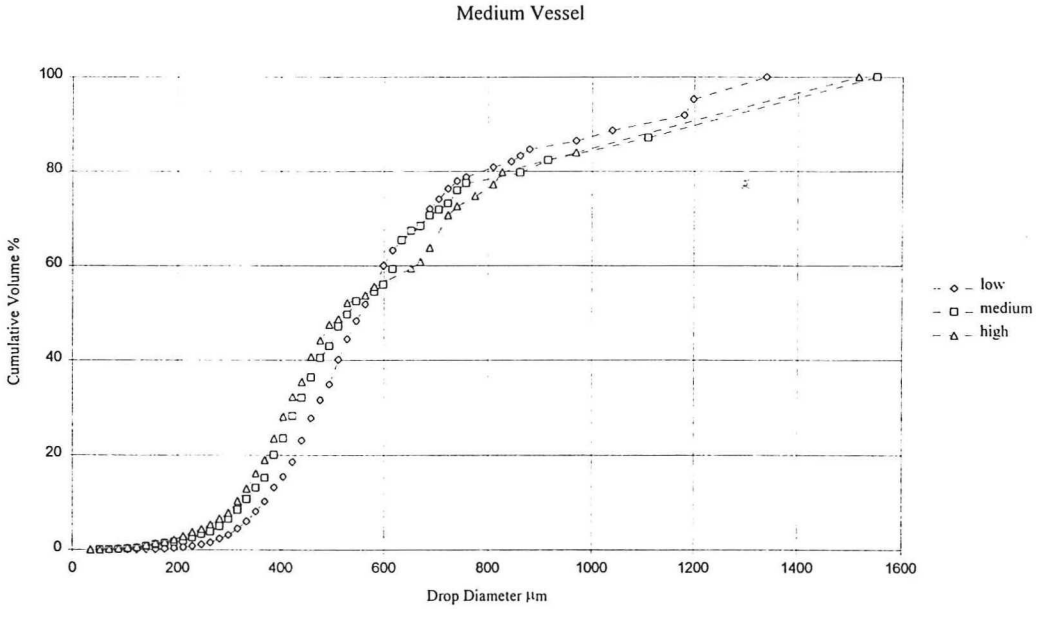

Figure 6.12 Cumulative volume distribution for three different power inputs in the medium vessel. Each sample consists of 500 drops measured.

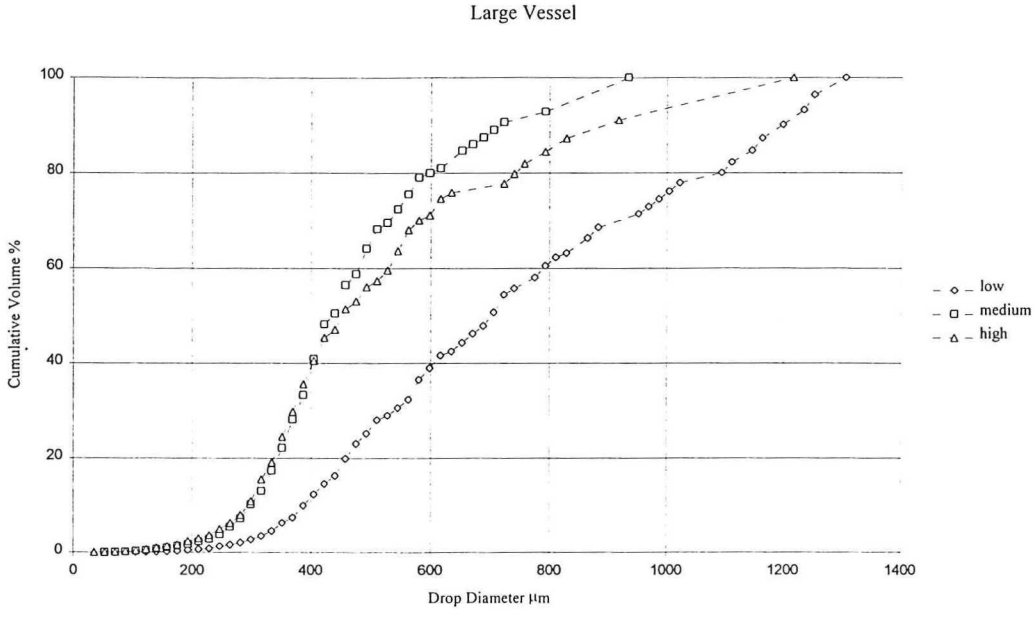

Figure 6. 13 Cumulative volume distribution for three different power inputs in the large vessel. Each sample consists of 500 drops measured.

In Fig. 6.10-6.13. it can be seen that the curves of the cumulative drop size distributions are not as smooth as one would expect of normal distributions. All curves show irregular behaviour in the region between 60% and 80%. This behaviour is more pronounced for measurements in dispersions with higher power input. The reason of the existence of this discontinuity may be that the drop size distribution is much more complicated than a normal distribution. In the previous section we treated bimodal distributions. The experimental results tend to indicate a certain bimodality.

It was concluded by [6] that the drop size of the dispersion is smaller if the power input is higher. This is not observed in this experiment. Only in Fig, 6.12. below the 60% region the latter effect is shown.

The drop size distribution at low power input in the large vessel, see Fig. 6.13., has a significantly different shape than the other distributions. An explanation for this is that the agitation speed did not create a complete dispersion. The scaling rules for minimum stirrer speeds given by van Heuven [8] ($N^{2.6}D^3$=C) and Nagata [13] (N^3D^2=C) do not apply in this case. The rules presumably are valid to keep the liquids *in* dispersion. To *create* a dispersion another mechanism is involved, lighter liquid has to be dispersed throughout the vessel from the surface. The best way to mix the liquids at the surface into the bulk of the vessel is with vortexing or entrainment. This is explained by Harnby et al. [7] for the mixing of floating solids. The Froude (Fr) number, see equation (2.2), is characteristic for vortexing. The scaling rule then would be N^2D=C. This would explain the significant different shape of the measurement in the large vessel with the low power input, as the value of Fr by far the lowest in this experiment. The values for Fr in the large vessel are 0.023, 0.055 and 0.132 for low medium and high power input respectively.

6.3 The effect of the different scales at constant specific power input

Hereafter are shown the cumulative volume distributions for the three different power-inputs: 0.20, 0.25, and 0.31 W/kg respectively. The 3 different measurements per graph are for the large, medium and small vessel. The measurements are the same as in section 6.2. they are presented in a different sequence.

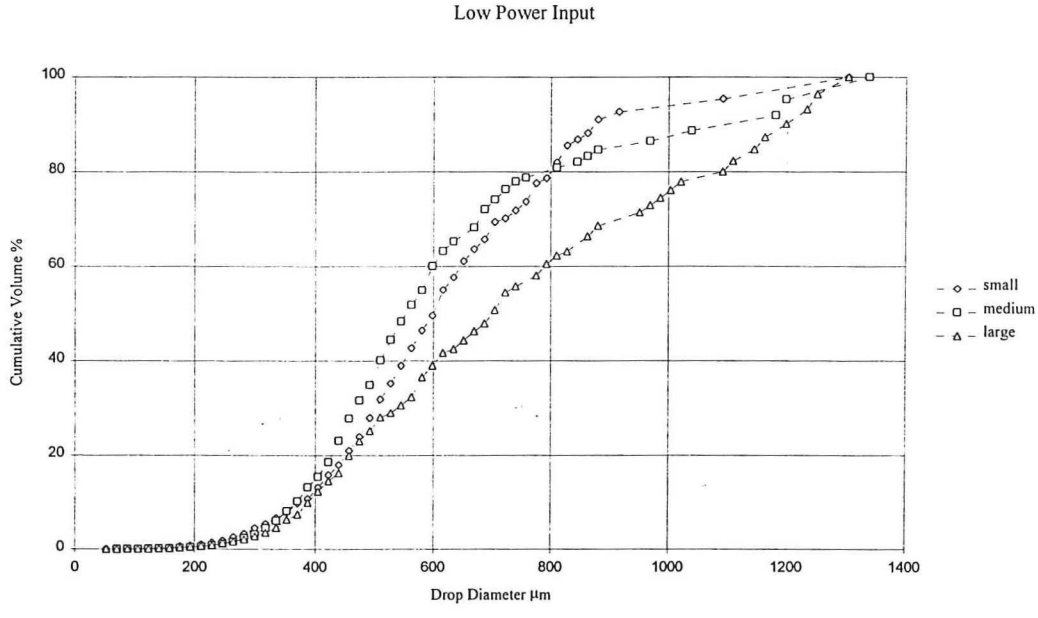

Figure 6.14 Cumulative volume drop size distribution for three different vessels with power input 0.20 W/kg.

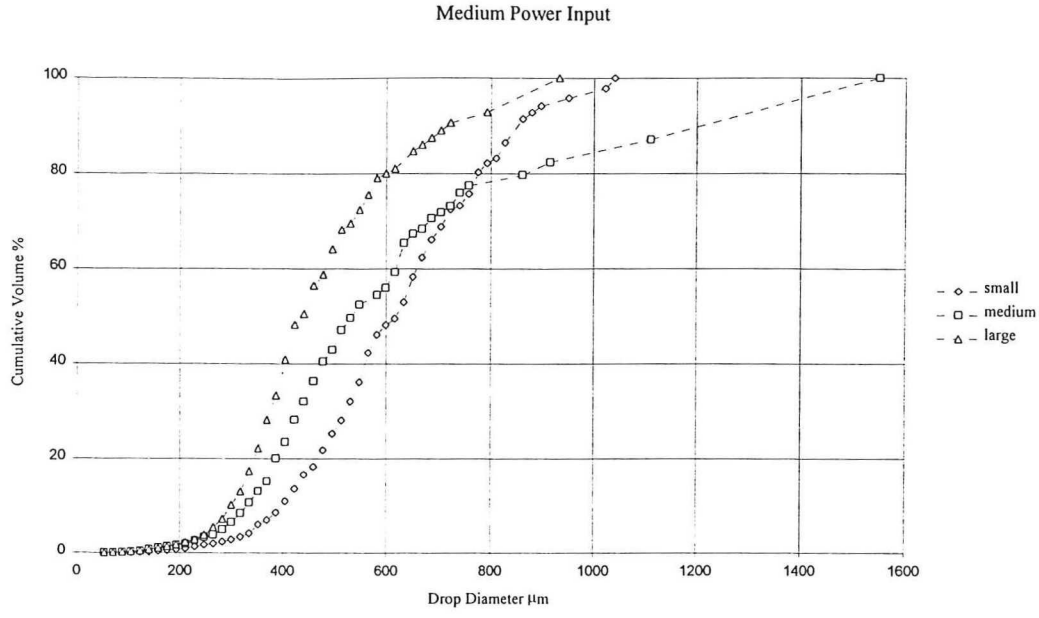

Figure 6.15 Cumulative volume drop size distribution for three different vessels with power input 0.25 W/kg.

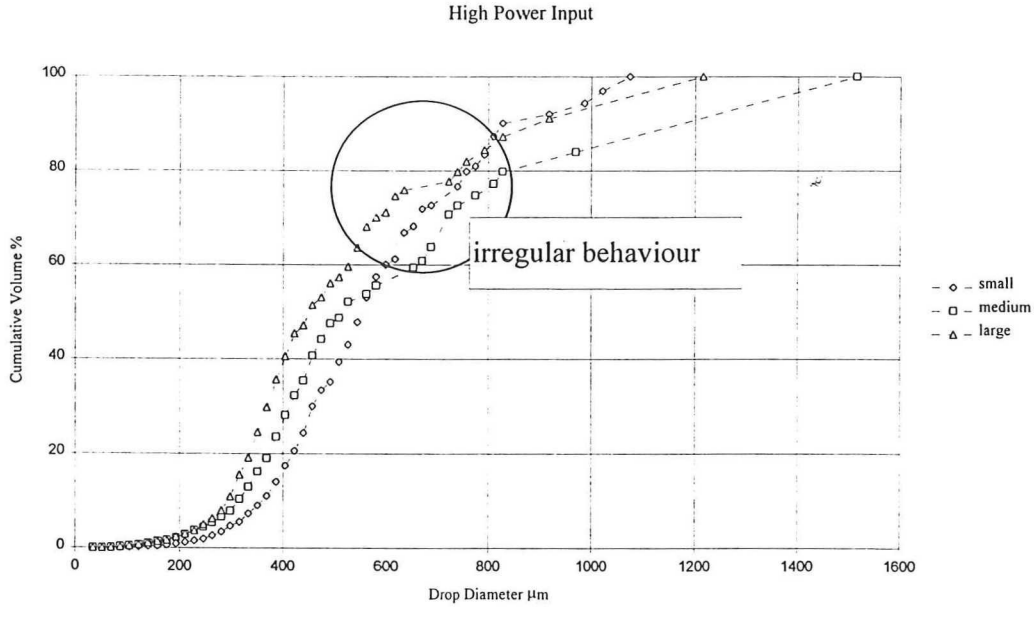

Figure 6.16 Cumulative volume drop size distribution for three different vessels with power input 0.31 W/kg.

In Fig. 6.14-6.16 it seems that for larger vessels the drop size becomes smaller. Except for the measurement in the big vessel for low power input. This effect was also concluded by [15]. They ascribed it to increasing turbulent power density in the inertial sub range for increasing diameter.

The error for the parameters d_{16}, d_{50} and d_{84} are determined with the Monte Carlo simulation program mentioned in section 5.3. This program calculates the standard deviation for the parameters d_{16}, d_{50} and d_{84}. This by simulating drops generated ad random from a particular number distribution. The number distribution is calculated from a normal volume distribution characterised with μ_d and σ_d. The standard deviation of the mentioned parameters is a function of the number of drops sampled in a measurement. The experimental parameter d_{50} is used as an input parameter for μ_d the mean drop diameter of the theoretical normal volume distribution. The average of d_{16}-d_{50} and d_{50}-d_{84} is used as the input parameter for σ_d, the standard deviation of the theoretical normal volume distribution. The minimum detectable drop size is set to 3 pixels and the simulation was based on 1000 repetitions of samples containing 500 drops. In figure 6.17 is an example of an experimental distribution with the standard deviation calculated with the simulation program as an error margin.

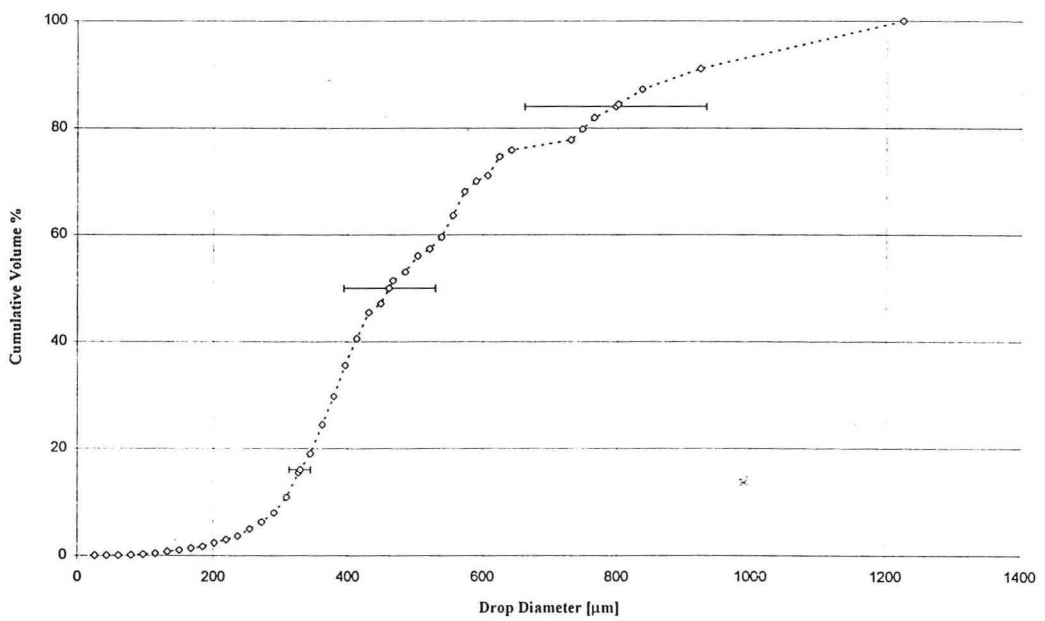

Figure 6.17 Cumulative volume drop size distribution of the large vessel with the high power input along with the error margins σ_p for the value of d_p.

Table 6.1. summarises the results of the scale experiments. The experimental values of d_p are depicted along with the simulated values of σ_p.

vessel	power-input	d_{84}	σ_{84}	d_{50}	σ_{50}	d_{16}	σ_{16}	d_{max}
small	low	433	18	609	29	829	56	1303
small	medium	446	16	628	23	823	41	1039
small	high	407	20	562	33	804	63	1074
medium	low	413	20	552	34	812	66	1197
medium	medium	382	58	539	150	1107	191	1550
medium	high	360	79	526	239	1312	232	1514
large	low	447	62	709	124	1148	196	1303
large	medium	338	15	445	25	657	48	933
large	high	328	32	461	67	798	136	1215

		d_{50}-d_{84}	$\sigma_{(50-84)}$	d_{16}-d_{50}	$\sigma_{(16-50)}$	$(d_{16}-d_{84})$ /2	d_{32}
small	low	176	23	220	47	198	559
small	medium	182	19	196	34	189	568
small	high	155	26	242	54	199	525
medium	low	139	26	260	54	200	533
medium	medium	158	111	567	124	363	517
medium	high	166	186	786	131	476	503
large	low	262	89	440	146	351	630
large	medium	107	19	212	38	160	428
large	high	132	49	338	105	235	443

Table 6.1. The values of the parameters that describe the drop size distribution of the scale experiments.

The value $(d_{16}-d_{84})/2$ can be interpreted as the width of the distribution with d_{50} as the mean drop size. The d_{32} values are calculated directly from the total set of from the measured drops. d_{max} is the biggest drop that was measured.

From table 6.1. it shows that the width of the right hand side (d_{16}-d_{50}) of the distribution is bigger than the width of the right hand side (d_{50}-d_{84}).

No firm conclusions can be made about the effect of the power input in one scale. The mean drop size does not significantly decrease with increasing power. The width of the distribution does not increase or decrease significantly with increasing power input. As stated earlier it seems that the mean drop size decreases with increasing vessel diameter, except for the measurement in the large vessel with the low power input.

6.4 Comparison with theory

Due to the addition of surfactants the interfacial tension varies with the total interface. The assumption can be made that by increasing the oil/water interface the density of the surface active molecules in the interface decreases. Resulting in an increasing surface tension of the interface of the drops. This effect has not been studied in this research. For the comparison of the experimental data

with the theoretical correlations found by Nishikawa [16], the variation of surface tension will be neglected.

In the next figure are depicted the experimental d_{32} values with error bars vs. the tank diameter, T. The simulated values σ_{50} are taken as the value for the error.

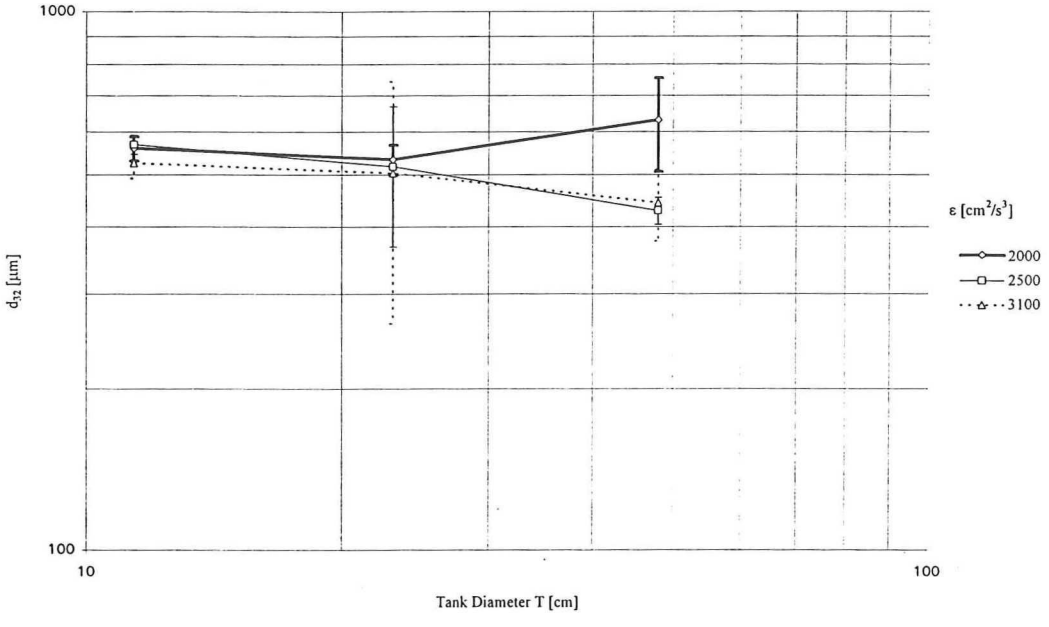

Figure 6.18 The values of d_{32} calculated from the experimental data vs the tank diameter for three different specific power inputs. The values for the error are calculated with the simulation program. The values for σ_{50} are used for this purpose.

From figure 6.18 it is impossible to determine a trend in the measurements. The error is too large for this. The error of the measurements can be decreased by measuring more drops when determining a drop size distribution. According to Nishikawa et al [16], the slope of the measurements in the graph should be -2/5 for the break-up region (lower power input) and -1/4 for the coalescence region (higher power input $\bar{\varepsilon}$ typically 2.5 m^2/s^3).

Before we try to compare the experimental values with the correlations (equation 2.12 and 2.13) an input parameter has to be determined. The value for the reference vessel diameter (D_0) was 0.25 m in the work of Nishikawa et al. This value corresponds with the diameter of their intermediate vessel. They used vessels with diameter 0.12, 0.16, 0.25 and 0.50 metre. The volume fractions (ϕ) of dispersed phase used in their experiment ranged from 0.005 to 0.3.

With 0.25 meter as a value for D_0 and with ϕ=0.5 the correlation for the break-up region corresponds the best, see figure 6.19. This is the correlation for the lower $\bar{\varepsilon}$ (typically 0.05 m^2/s^3). It proved impossible to determine the exponent of $\bar{\varepsilon}$ from the experimental data as the error for d_{32} is relatively high.

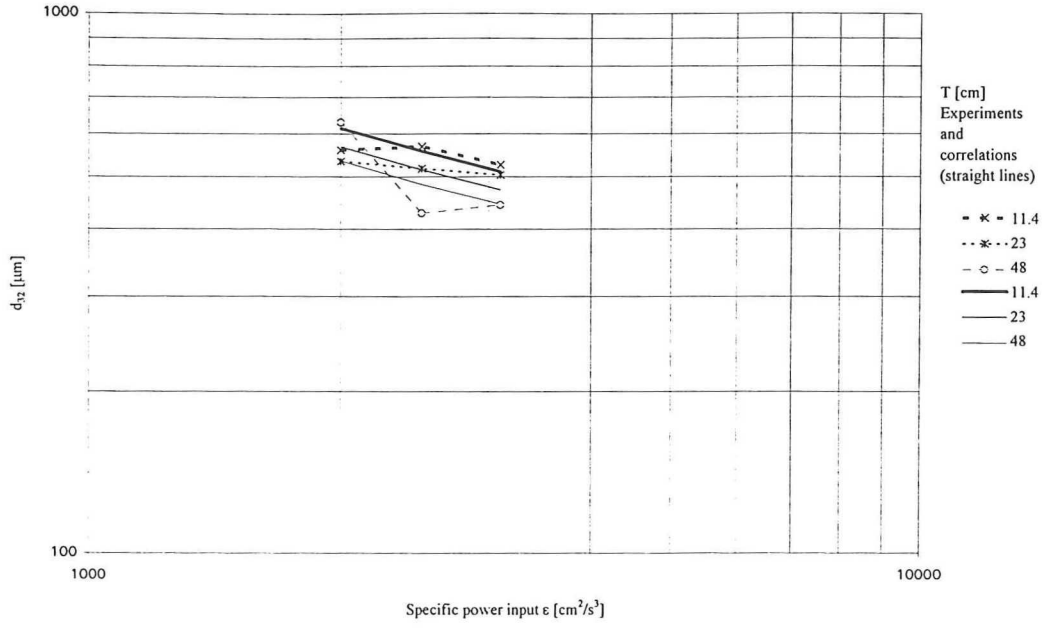

Figure 6.19 The values of d_{32} calculated from the experimental data vs the specific power input for three different vessel diameters. Along with the correlation for the break up region by Nishikawa et al.

The correlation for the coalescence region (for higher $\bar{\varepsilon}$) produced an increasing d_{32} for increasing impeller diameter D. This trend does not correspond with the experiments and is neither observed by Nishikawa et al. This trend shows in the correlation (2.12) for a high fraction dispersed phase along with a low tank reference diameter.

The experiments did not correspond very well with the correlations of Nishikawa et al. A number of reasons can be given to explain the difference between the correlation and the experiments:

- First of all, the number of drops used to determine a value for d_{32} was too little. The width of the drop size distribution was bigger than expected. According to the simulation programme, a typical sample for this kind of distribution should hold 4000 drops. The number of 4000 drops is calculated with the simulation program, with μ_d=600 µm and σ_d=250 µm, the minimum detectable drop size is set to 4 pixels. With 4000 drops the standard deviation σ_{16} for d_{16} is 2 pixels or 35 µm. The values for σ_{50} and σ_{84} are smaller than 35 µm.

- Secondly the surface tension is not known for each experiment. It will be difficult to measure the surface tension as it is a function of the total interfacial area.

- Thirdly, the correlations are valid for a volume fraction ranging between 0.005 and 0.3. It is not straightforward that the correlations are valid for values of ϕ higher than 0.3.

- And finally, the limited $\bar{\varepsilon}$ range combined with the high inaccuracy in d_{32} give rise to inaccuracy while fitting a correlation This problem is solved by increasing the range of the specific power input and the measurements. In this way it may be possible to distinguish different regions as mentioned by Nishikawa et al.

7 Conclusions and recommendations

7.1 Conclusions

- The drop size measurement system developed in this work enables detailed observation of the structure of a dispersion, revealing the presence of droplets-in-drops and distinguishing between air bubbles and liquid drops. This method can distinguish drops ranging from 50 μm to 1.6 mm with an error of 50 μm. In principle it is possible to measure everywhere in the vessel in any direction. Other advantages of this method are the relatively high frequency of data acquisition (50 frames a second).
- The statistical simulation program developed is a useful tool to determine the statistical accuracy of the measured width of a distribution. It is possible to calculate the number of drops in a sample needed for determining the width of an estimated distribution, within a given statistical accuracy.
- The mean drop size of the distribution decreases with increasing vessel diameter and constant specific power input.
- Different specific power input at different scales did not result in a significant change in the width of the distribution.
- The minimum agitation speed for dispersions does not scale on the basis of specific power input.
- The drop size distribution is not normal shaped. This shape is more pronounced for dispersions with a higher power input. An explanation for this effect could be that the drop size distribution is a combination of two effects: coalescence and break-up.
- Measurements with large variation in power input are impossible with the current experimental set-up. A low power input results in laminar flow, while a higher power input results in vortexing.

6.2 Recommendations

- The influence of surfactants is not understood very well. More research should be done to test the reproducibility of experiments using surfactants. The comparison with theory is not straightforward as interfacial tension may vary with the total interface.
- A volume drop size distribution is very sensitive to large drops. The accuracy of the drop size distribution measurement is larger if the smallest detectable drop is set to roughly 1/3 of the mean diameter, as the smallest drops have no significant contribution to the total volume. In this way more large drops are measured increasing the accuracy of the volume distribution if the distribution consists of the same number of drops.

- To be able to change the specific power input significantly, the vessels have to be altered in such way that increase the specific power input does not initiate vortexing. A lid on the vessel sealing the dispersion from the atmosphere may be a solution for this problem.
- More research on the different time scales for coalescence and break-up could enhance the understanding of the different mechanisms.

References

1. Beek, W.J., Muttzall, K.M.K., 1983, Transport Phenomena, John Wiley & Sons Ltd.
2. Brown, D.E., Pitt, K., 1972, Drop size distribution of stirred non-coalescing liquid-liquid system, Chem. Eng. Sci., 27, pp. 577-583.
3. Calabrese, R.V.,Chang,T.P.L., Dang, P.T.,1986,Drop Breakup in Turbulent Stirred-Tank Contractors, AIChE Journal, Vol. 32, No. 4,pp. 667-676.
4. Chatzi, E., Boutris, J., Kiparissides, C., 1991, Ind. Eng. Chem. Res., Vol. 30, No. 3.
5. Fennell Evans,.D., Wennerstrom, H,The Colloidal Domain where physics chemistry biology and technologie meet,VCH
6. Godfrey, J.C., Obi, F.I.N., Reeve, R.N.,1989, Measuring Drop Size in Continuous Liquid-Liquid Mixers, Chemical Engineering Progress,
7. Harnby, N., Edwards, M.F., Nienow, A.W., Mixing in the process Industries, Butterworths series in the process industries.
8. Heuven, J.W. van, Beek, W.J., 1971, Power input, drop size and minimum stirrer speed for liquid-liquid dispersions in stirred vessels, Proceedings Internationa Solvent Extraction Conference, Vol 1, paper 51, pp: 70-81.
9. Jansen, L.P.B.M., Warmoeskerken, M.M.C.G., 1991, Transport Phenomena Data Companion, Delftse Uitgevers Maatscappij b.v.
10. Konno, M., Aoki, M., Saito, S., 1983, Scale effect on breakup process in liquid-liquid agitated tanks, Journ. of Chem. Eng. of Japan, Vol. 16, No. 4, pp. 312-319.
11. Mersmann, A., Grossman, H., 1982, Dispersion of immiscible liquids in agitated vessels, Int. Che. Eng. Vol. 22, No. 4, pp 581-590.
12. Morgan, B.J.T., 1984, Elements of simulation. Texts in statistical science, Textbook(Chapman & Hall).
13. Nagata, S,1975, Mixing, Principles and application,John Wiley & Sons Ltd.
14. Nishikawa, M., Okamoto, Y., Hashimoto, K., Nagato, S.,1976, Turbulent energy spectra in baffled mixing vessels, Journ. of Chem. Eng. of Japan, Vol.9, No. 6, pp. 489-494.
15. Nishikawa, M., Mori, F., Fujieda, S., 1987, Average drop size in a liquid-liquid phase mixing vessel, Journ. of Chem. Eng. of Japan, Vol. 20, No. 1, pp. 82-88.
16. Nishikawa, M., Mori, F., Fujieda, S., Kayama, T., 1987, Scale-up of liquid-liquid phase mixing vessel, Journ. of Chem. Eng. of Japan, Vol. 20, No. 5, pp. 454-459.
17. Okufi, S., Perez de Ortiz, E.S., Sawistowski, H.,1990, Scale-up of liquid-liquid dispersions in stirred tanks, Can. J. Chem. Eng. Vol. 68, pp.400-406

19. Pacek, A.W., Nienow, A.W., 1995, Measurement of drop size distribution in concentrated liquid-liquid dispersions: video and capillary texhniques, Trans IChemE, Vol 73, Part A, pp 512-518.

20. Pacek, A.W., Moore, I.P.T., Nienow, A.W., 1994, Video technique for measuring dynamics of liquid-liquid dispersion during phase inversion, AIChE Journal, Vol. 40, No. 12.

21. PAR, Personal Animation Recorder user manual, System Ver. 1.

22. Scil_image User anual, version 1.3, by TNO/TPD.23. Tanaka, M., Hosogai, K., 1990, Suspension plymerization of styrene with circular loop reactor, Journ. of applied polymer Sci. Vol. 39, pp. 955-966.

24. Tjaberinga, W.J., Boon, A., Chesters, A.K., Model experiments and numerical simulations on emulsification under turbulent conditions, Chem. Eng. Sci., Vol. 48, No. 2, pp285-293.

25. Turbo pascal V5 User manual, Borland

26. Ward, J.P., Knudsen, J.G., 1967, AIChE Jl, 13, 356.

27. Yi, J., Tavlarides, L., 1990, Model for Hold-up measurements in liquid dispersions using an ultrasonic technique, Ind. Eng. Chem. Res., Vol. 29, No. 3.

List of symbols

Normal symbols

a	impeller angle	°
a_i	interfacial area	m^2/m^3
A_b	drag surface of fluid	m^2
c	bottom clearence	m
cb	baffle clearence	m
ci	impeller distance	m
c_w	class width	m
C	constant	-
C_d	drag coefficient	-
C_f	calibration factor	-
d	drop diameter	m
da	axis diameter	m
d_i	diameter of the i-th particle	m
d_j	diameter of drops in the j-th class	m
d_p	diameter at (100-p)% of cumulative volume fraction curve of droplet diameter distribution	m
d_{16}	diameter at 84% of cumulative volume fraction curve of droplet diameter distribution	m
d_{32}	Sauter Mean Diameter	m
d_{50}	diameter at 50% of cumulative volume fraction curve of droplet diameter distribution	m
d_{84}	diameter at 16% of cumulative volume fraction curve of droplet diameter distribution	m
D	impeller diameter	D
D_i	image diameter	pixels
D_m	mask diameter	pixels
D_{mm}	diameter of the measurement microscope	m
D_{px}	pixel diameter	pixels
$f_c(d)$	cumulative volume density function	-
$f_n(d)$	number density function	-
$f_v(d)$	volume density function	-
F	drag force of fluid	N
g	gravitational acceleration	m/s^2
gb	baffle gap	m
hs	submergement impeller	m
H_l	liquid height	m
lb	baffle lenght	m
M	torque	N·m
n	number of particles on a sample	-
N	impeller rotational speed	1/s
P	power input	W
q	number of bins ro classes	-

Δt	time between measurements	s
tb	baffle thickness	m
ti	impeller thickness	m
T	tank diameter	m
T_o	reference tank diameter	m
v	characteristic velocity	m/s
V	volume	m^3
V_l	liquid volume	m^3
wb	baffle width	m
wi	impeller width	m
x	scale of turbulent eddy	m

Greek symbols

ρ	density of fluid	kg/m^3
ϕ	volumetric fraction of dispersed phase	-
η	dynamic viscosity	N·s/m
μ_d	average drop size	m
σ_d	standard deviation af a drop size distribution	m
λ_f	dissipation scale of turbulence	m
τ	surface tension	N/m
ν	kinematic viscosity	m^2/s
$\bar{\varepsilon}$	average energy dissipation rate	m^2/s^3

Dimensionless numbers

Fr	Froude number	-
Po	Power number	-
Re	Reynols number	-
We	Tank Weber number	-

Apendix A

Some typical images of Endoscope-1.

21

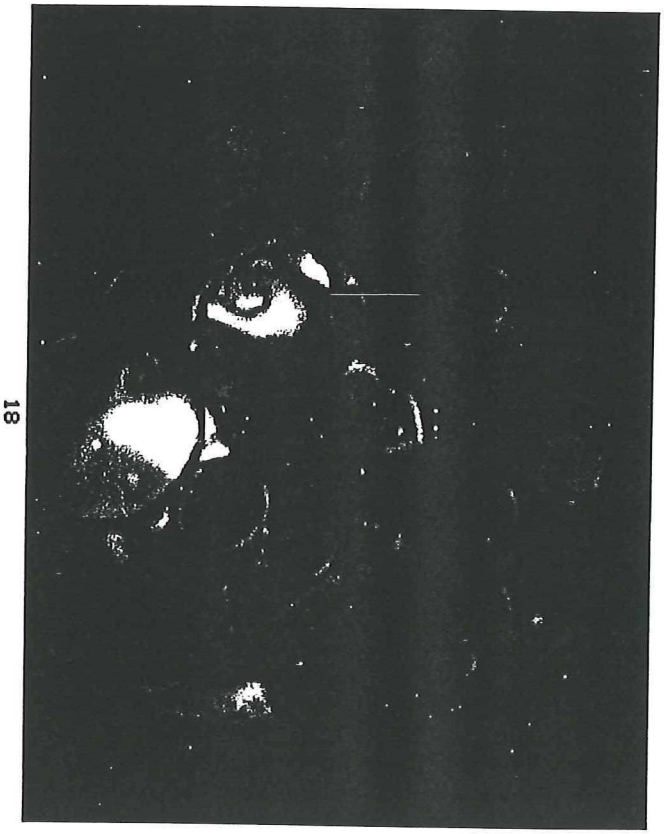

18

12

13

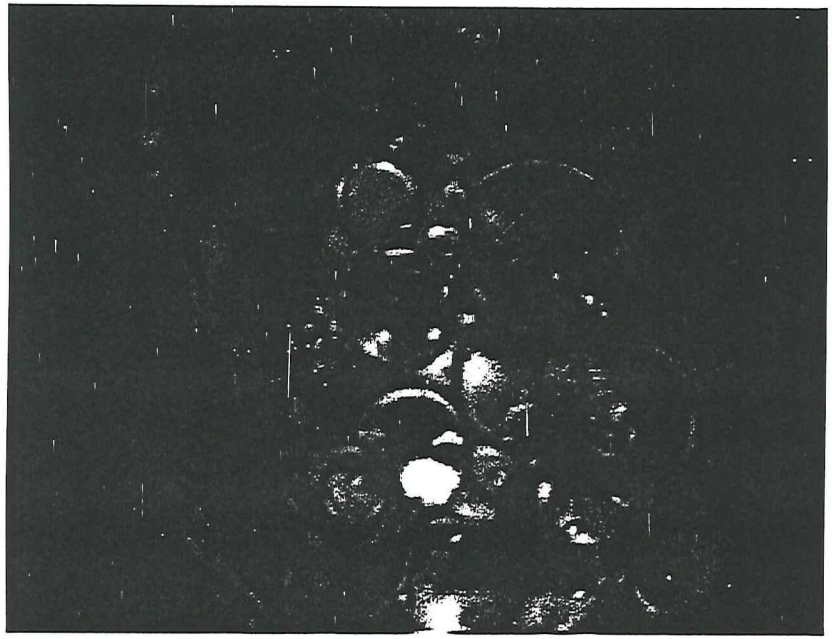

15

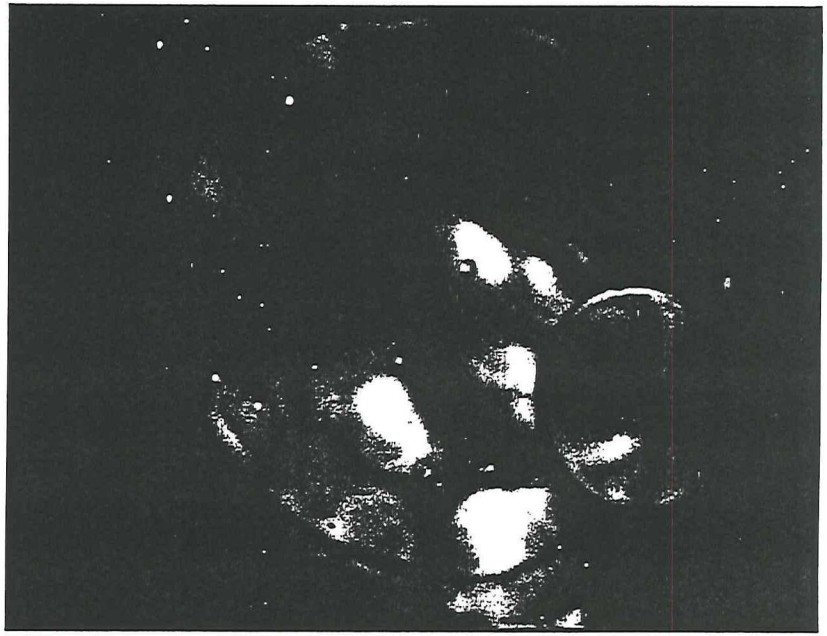

16